3-2003

Cold-Flow Testing of a Subscale Model Exhaust System for a Space-Base Laser

Ian S. Bautista

COLD-FLOW TESTING OF A SUBSCALE MODEL EXHAUST SYSTEM FOR A SPACE-BASED LASER

THESIS

Ian S. Bautista, Captain, USAF

AFIT/GAE/ENY/03-1

DEPARTMENT OF THE AIR FORCE
AIR UNIVERSITY

AIR FORCE INSTITUTE OF TECHNOLOGY

Wright-Patterson Air Force Base, Ohio

The views expressed in this thesis are those of the author and do not reflect the official policy of position of the United States Air Force, Department of Defense, or the United States Government.

AFIT/GAE/ENY/03-1

COLD-FLOW TESTING OF A SUBSCALE MODEL EXHAUST SYSTEM FOR A SPACE-BASED LASER

THESIS

Presented to the Faculty

Department of Aeronautical and Astronautical Engineering

Graduate School of Engineering and Management

Air Force Institute of Technology

Air University

Air Education and Training Command

In Partial Fulfillment of the Requirements for the

Degree of Master of Science in Aeronautical Engineering

Ian S. Bautista, BS

Captain, USAF

March 2003

AFIT/GAE/ENY/03-1

COLD-FLOW TESTING OF A SUBSCALE MODEL EXHAUST SYSTEM FOR A SPACE-BASED LASER

Ian S. Bautista, BS
Captain, USAF

Approved:

Milton E. Franke Ph.D. (Chairman)	11 Mar 2003 Date
LtCol Montgomery Hughson Ph.D. (Member)	12 Mar 2003 Date
Paul I. King Ph.D. (Member)	13 Mar 03 Date

Acknowledgments

First and foremost, I would like to thank my loving family for their wonderful support. I especially want to thank my wife, who always acted interested while listening to me ramble about a subject she has no interest in. A hearty thank you goes to my advisor, Dr. Milton Franke, who always gave me encouragement to move in the right direction. A late Christmas card will be sent to Jan LeValley and Condie Inman from the AFIT machine shop for being a year round Santa Claus. All of their presents have been masterpieces. And finally, a special thanks to Andy Pitts, my lab technician. Without him, this thesis would have never taken off. His lab expertise and great personality have made this thesis feasible and definitely enjoyable.

Ian S. Bautista

Table of Contents

Page

List of Figures

Page

Page

List of Tables

Page

List of Symbols

Symbol	Definition	Units
English Notation		
A	cross-sectional area, perpendicular to flow	m
a	speed of sound	m/s
B	bias error	
D	diameter	m
ds	change in entropy	J/kgK
f	Darcy friction factor	
h	head loss	m^2/s^2
K	loss coefficient	
L	length	m
M	Mach number	
$\dot{m}$	mass flow rate	kg/s
p	pressure	Pa
R	specific gas constant	J/kgK
T	temperature	K
t	time	sec
U	x-direction component of velocity	m/s
V	velocity	m/s
w	uncertainty	
Greek Notation		
β	shock wave angle	deg
γ	ratio of specific heats	
ρ	density	kg/m^3
θ	turning angle	deg
ν	kinematic viscosity	m^2/s
μ	mach wave angle	deg
Λ	volume	m^3
Subscripts/Superscripts		
*	critical dimension	
o	stagnation	
T	combined (total)	
l	loss	

h	wetted
n	normal component
t	tangential component
1	upstream location
2	downstream location

Abstract

The purpose of this research was to continue a study of gas-dynamic phenomena that occurred in stacked cylindrical rings of nozzles and an exhaust manifold as reported by Captain Scott Bergren in 2002. The rings and exhaust manifold were part of a 1/5-scale model of one quadrant of the conceptual Space Based Laser Integrated Flight Experiment (SBL IFX) gas dynamic laser. This model was mated to a blow-down/vacuum wind tunnel and consisted of a nozzle array, centerbody, supersonic diffuser, and a transition structure to mate the vacuum and test section. During Capt Bergren's research, supersonic flow was found to only last for 0.2 seconds from wind tunnel startup. The short duration of the supersonic flow was due to the transition structure being too small and not being able to "swallow" the shock wave.

The objectives of this research were to remodel the transition structure and evaluate the test section to see if simulation of the expected fluid flow properties in the conceptual SBL IFX design was possible using cold-flow. The transition structure was remodeled to capture the entire vacuum line entrance area while still mating to the diffuser exit. Using rapid data acquisition and schlieren photography, results indicated that supersonic flow lasted for approximately 10 seconds from startup. During this time, a well-defined oblique shock wave inside the optical cavity attached to the leading edge of the centerbody, where the flow reached a velocity of Mach 2.8.

COLD-FLOW TESTING OF A SUBSCALE MODEL EXHAUST SYSTEM FOR A SPACE-BASED LASER

I. Introduction

Background

Lasers have been tested as an effective weapon against missiles since 1973. During that time, the Mid Infrared Advanced Chemical Laser (MIRACL) was developed and first tested against tactical missiles and drone aircraft (Federation, 2002). This laser weapon concept is currently pursued with the Airborne Laser Program (ABL), which fits a Chemical Oxygen Iodine Laser (COIL) into a Boeing 747 aircraft. Its objective is to destroy ballistic missiles during the boost phase of their flight.

The Space-Based Laser Integrated Flight Experiment (SBL IFX) planned to build on this concept to investigate the possibility of placing gas dynamic lasers (GDL) in space to accomplish the same objective through space rather than aircraft. The SBL-IFX program was funded by both the U. S. Air Force and the Ballistic Missile Defense Organization (BMDO). The contract was with three partners consisting of The Boeing Company, Lockheed-Martin Corporation, and TRW, Inc. The SBL-IFX program aims to provide a means of improving beam quality and phasing of multiple chemical laser gain generators, to demonstrate the capability of a hydrogen fluoride (HF) laser, and to integrate the components of an SBL into a ground experiment to demonstrate operation of the high power elements of a space-based laser. The internal fluid dynamics associated with this high power gas dynamic laser are the focus of this study.

The power generated in the SBL IFX is a result of an exothermic reaction of hydrogen and dissociated fluorine. An array of nozzles accelerates the fluorine

molecules supersonically. Molecular hydrogen is then injected into the supersonic expansion inside the divergent section of the nozzle to enable good mixing and efficient reaction with the fluorine to produce the vibrationally inverted HF molecules required for lasing. The need for supersonic flow here is three fold:

1. The chemical reaction needs to occur quickly for lasing to occur, since the faster the mixing time the quicker the chemical reaction.
2. High temperatures destroy the lasing process and isentropic, supersonic expansion is a way to produce low temperatures conducive for lasing.
3. Faster fluid allows more power to be extracted from the fluid flow (Perram, 1999).

The subsequent optical energy inside the lasing cavity is then extracted from the supersonic flow. The gain generation assembly can achieve higher power by simply stacking more rings.

The quality of the laser beam is highly dependent on the flow characteristics within the lasing cavity. Low density, pressure and temperature are all needed for a high quality beam. A low density reduces the deactivation of excited HF molecules, and a low pressure is better for molecular diffusion. Also, a low temperature allows for better laser inversion which results in a higher gain. A high Mach number is consistent with all of these effects, and is therefore desired at the nozzle exit plane and throughout the lasing cavity. Shock waves and boundary layer separation, however, are sources of beam distortion and result in less energy that may be drawn from the flow. Therefore, flow homogeneity is strongly desired inside the lasing cavity (Lohn, 2001).

Problem Statement

TRW was responsible for the power generation portion of the SBL IFX. This segment of the SBL IFX is where the population inversion occurs causing the initial lasing. Currently, TRW has designed a nozzle array and diffuser that will theoretically create a laser in the megawatt class. Two-dimensional, computational fluid dynamics (CFD) by TRW has yielded preliminary results for the performance of the proposed design.

Experimental data is desired to verify these CFD results. The current cold-flow subscale model of the proposed design can be redesigned to simulate the flow characteristics of the computational results. Once this is accomplished, the flow characteristics of the model can be examined to determine the effectiveness of a full scale laser.

Objectives

This research effort has two major objectives:

1. The previous test facility was a one-fifth scale, 90 deg segment of the proposed TRW laser generator. The first objective was to remodel the previous test facility so that it would be capable of investigating flow conditions in a simulated laser nozzle assembly and lasing cavity using cold-flow. The facility was designed to be modular for the purposes of testing various geometries. The first objective was accomplished by redesigning the transition structure mating the model to the existing blow-down wind tunnel. The previous transition structure contained a rectangular exit area and mated to a circular vacuum line entrance. Nearly two-thirds of the vacuum line

entrance area was lost by using the rectangular exit for the transition structure. By mating the circular vacuum line with a circular transition exit, most of the diffuser cross-sectional area was recovered. This will be explained in further detail in Chapter 3.

2. The second objective was to examine the flow properties of the scaled nozzle/diffuser system using time based pressure measurements and schlieren photography. Experimental data from this facility can then be compared to the CFD results from TRW. The second objective was accomplished using a rapid data acquisition system to obtain static pressure readings at various locations and a basic schlieren photography setup for visual analysis of the flow including shock waves and areas of separation.

Summary of Current Knowledge

Current knowledge of gas dynamic lasers has matured through the development of the Alpha High Energy Laser. Because the design of the MIRACL was intended for sea level operation, it did not achieve the optimum efficiency necessary for space-based operation. Therefore, the Defense Advanced Research Projects Agency (DARPA) launched the Alpha laser program, with the goal of developing a megawatt level SBL that was scaleable to more powerful weapon levels and optimized for space operation. Like the SBL IFX proposed laser design, the Alpha laser also contained stacked cylindrical rings of nozzles used for reactant mixing. In 1991, the Alpha laser demonstrated megawatt class power levels similar to MIRACL, but in a low pressure, space operation environment. This demonstrated that multi-megawatt, space-compatible lasers could be built and operated (Federation, 2002; Greenwald, 2000).

In the study conducted by Captain Scott Bergren which preceded this research, the 1/5-scale model was fabricated and mated to a blow-down/vacuum combination wind tunnel. The primary components of the test apparatus consisted of a nozzle array, optical cavity, supersonic diffuser, centerbody, and transition section. The throat height of a single nozzle was 1 mm and the expansion ratio was two. A transition structure was designed to attach the subscale model to the wind tunnel facility vacuum line and was not part of the SBL IFX design (Bergren, 2002).

Using rapid data acquisition and schlieren photography, the fluid velocities in the diffuser were determined to become subsonic after a transient time interval of 0.2 seconds from wind tunnel startup for a 30 second long test. During this transient time interval, a well-defined, attached oblique shock wave was observed off the leading edge of the centerbody within the optical cavity of the diffuser, and the fluid in the optical cavity reached an observed maximum Mach number of 2.7 (Bergren, 2002).

The flow characteristics observed during the transient time period are very conducive to high beam quality, but the 0.2 second duration is far too brief for lasing activity. The short duration can be attributed to the exit area of the transition structure, which was too small to "swallow" the normal shock that propagated down the length of the test section (Bergren, 2002).

TRW has performed computer modeling for two-dimensional flow and the results exhibited lasing cavity boundary layer separation sensitive to small changes in back pressure. Furthermore, the results showed the lasing cavity free of shock waves and interactions which would degrade lasing performance.

Method

In order to accomplish the first objective, the transition structure of the test facility required re-designing. The following questions needed to be answered:

1) What design/shape should the structure be to obtain the most exit area at the vacuum line entrance?
2) Where should the transition section mate to the vacuum line?

Once the transition structure had been built and connected to the test section and vacuum line, the following general method was used to obtain the necessary data to complete the research's objectives.

1) Run the wind tunnel with pressure transducers at different locations throughout the length of the diffuser
2) Obtain schlieren images inside the optical cavity and farther back above the centerbody
3) Record wall static pressure at transducer locations
4) Calculate Mach numbers using schlieren images and pressure readings
5) Observe shock patterns in both schlieren locations

This thesis is organized to allow the reader to understand why certain design decisions were made to remodel the first test facility for the SBL IFX and what procedures and equipment were used throughout the experimentation. The theory chapter explains the fundamentals of compressible gas dynamics and turbulent jets, which is needed to understand the flow field inside the lasing cavity and diffuser.

The Methodology chapter explains the procedures and equipment used, and how one could duplicate the experiment to reach the same results. Discussion is given as to why certain procedures were used to accomplish different tasks.

The Results chapter presents and discusses the data collected from the experiments. These are presented in mainly in graphs and pictures, so that the reader may visually understand trends in the flow.

Lastly, a Conclusions and Recommendations chapter closes the thesis by explaining the relevance and applications for the findings documented in this study. Additionally, as the section title suggests, recommendations are made as to what paths future endeavors in this work should follow to achieve more in-depth results with possibly higher accuracy.

II. Theory

Quasi-One-Dimensional-Flow

The distinction between one-dimensional flow and quasi-one dimensional flow is that one-dimensional flow is treated as strictly constant-area flow, where as quasi-one-dimensional flow allows the cross-sectional area to vary with distance x, as seen in Figure 2.1. This is the type of flow which will be analyzed in the supersonic nozzle array.

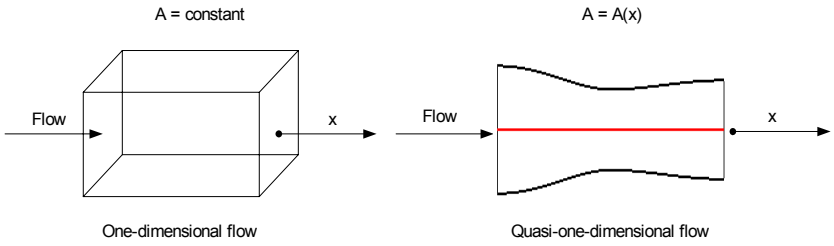

Figure 2.1 Comparison of One-Dimensional and Quasi-One-Dimensional Flows

The mass flow of a thermally and calorically perfect gas through a choked supersonic nozzle is given in terms of stagnation properties by

$$\dot{m} = \frac{p_0 A^*}{\sqrt{T_0}} \sqrt{\frac{\gamma}{R}\left(\frac{2}{\gamma+1}\right)^{(\gamma+1)/(\gamma-1)}} \tag{1}$$

where the Mach number at the throat is known to be unity (Anderson, 1990:184).

Assuming steady flow, conservation of mass can be used to find the instantaneous Mach number at any cross-section. Once the static properties and area are known at a certain location, a simple derivation of $\dot{m} = \rho A V$ and a transformation of velocity to Mach number gives

$$M = \frac{\dot{m} RT}{pAa} \tag{2}$$

where a is the speed of sound and represented as $\sqrt{\gamma RT}$ for a perfect gas and A is the cross-sectional area at the pressure transducer location (Anderson, 1990).

Mach number can also found using pressure relationships from isentropic flow properties. If both total and static pressure are known at a certain location, then Mach number can be calculated. This is especially helpful when calculating Mach number at the exit plane of a supersonic nozzle.

$$M = \sqrt{\frac{2}{\gamma - 1}\left(\frac{p_0}{p}^{\frac{\gamma-1}{\gamma}} - 1 \right)} \tag{3}$$

Oblique Shock Waves

The geometry of an oblique shock wave is shown in Figure 2.2 below.

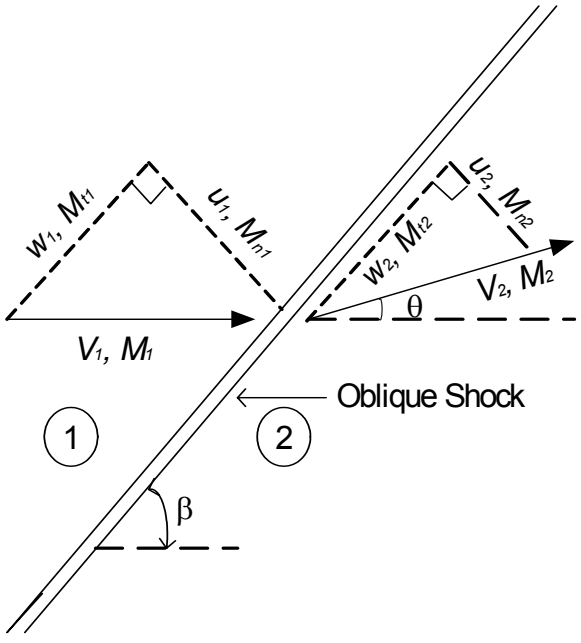

Figure 2.2 Oblique Shock Wave Geometry

The velocity and corresponding Mach number upstream and horizontal to the oblique shock are known as V_1 and M_1, respectively. A deflection angle, θ, behind the shock turns the flow parallel to the angle. This velocity and corresponding Mach number are known as V_2 and M_2, respectively. The oblique shock makes a wave angle, β, due to the turning of the flow. The components of V_1 perpendicular and parallel, respectively, to the shock are u_1 and w_1; the analogous components of V_2 are u_2 and w_2, as shown in Figure 2.2. Therefore, we can consider the normal and tangential Mach numbers ahead of the shock to be M_{n1} and M_{t1}, respectively; similarly, we have M_{n2} and M_{t2} behind the shock. The tangential component of the flow velocity is preserved across the oblique shock wave (Anderson, 1990:104).

The Mach number in region 1 can be derived from a known deflection and wave angle. This relationship, otherwise known as the θ–β-*M relation*, is shown in the equation below.

$$\tan\theta = 2\cot\beta\left[\frac{M_1^2\sin^2\beta - 1}{M_1^2(\gamma + \cos 2\beta) + 2}\right] \tag{4}$$

These results are well published and often plotted for a wide range of wave angles versus deflection angles with Mach number as a parameter. These relations are vital to an analysis of oblique shocks, and the following should be noted (Anderson, 1990:107):

1. For any given M_1, there is a maximum deflection angle θ_{max}. If $\theta > \theta_{max}$, then no solution exists for a straight oblique shock wave. Instead, the shock will be curved and detached.
2. For any given $\theta < \theta_{max}$, there are two values of β predicted by the θ–β-*M* relation for a given Mach number. Because changes across the shock are more severe as β

increases, the large value of β is called the strong shock solution. The small value of β is called the weak shock solution. In nature, the weak shock solution is favored, and usually occurs.

3. If θ = 0, then β = π/2 (corresponding to a normal shock) or β = μ (corresponding to a Mach wave), where $\mu = \sin^{-1}\frac{1}{M}$.

4. For a fixed deflection angle θ, as the free-stream Mach number decreases from high to low supersonic values, the wave angle increases.

After the upstream Mach number is established, the normal component can be found using

$$M_{n_1} = M_1 \sin\beta \tag{5}$$

With the normal component of the upstream Mach number, normal shock relations can be used to find properties such as static pressure behind the oblique shock wave.

$$\frac{p_2}{p_1} = 1 + \frac{2\gamma}{\gamma+1}\left(M_{n_1}^2 - 1\right) \tag{6}$$

This equation shows that the pressure of a fluid will rise as supersonic flow passes through a stationary shock wave.

Mach number behind the wave is also found using the normal velocity component upstream.

$$M_{n_2}^2 = \left[\frac{M_{n1}^2 + [2/(\gamma-1)]}{[2\gamma/(\gamma-1)]M_{n1}^2 - 1}\right] \tag{7}$$

Once the normal velocity is found, the total Mach number behind the shock wave is calculated using

$$M_2 = \frac{M_{n_2}}{\sin(\beta - \theta)} \tag{8}$$

Prandtl-Meyer Expansion Waves

An expansion wave is formed when supersonic flow is turned away from itself. This action is directly opposite of an oblique shock wave where the flow is turned into itself as explained above. Some qualitative aspects of flow through an expansion wave are itemized as follows (Anderson, 1990:131):

1. An expansion corner is a means to increase the flow Mach number.
2. The pressure, density, and temperature decrease through an expansion wave.
3. The expansion fan itself is a continuous expansion region, composed of an infinite number of Mach waves, bounded upstream by μ_1 and downstream by μ_2 (see Figure 2.3), where $\mu_1 = \arcsin(1/M_1)$ and $\mu_2 = \arcsin(1/M_2)$.
4. Streamlines through an expansion wave are smooth curved lines.
5. Since the expansion takes place through a continuous succession of Mach waves, and $ds = 0$ (change in entropy) for each Mach wave, the expansion in isentropic.

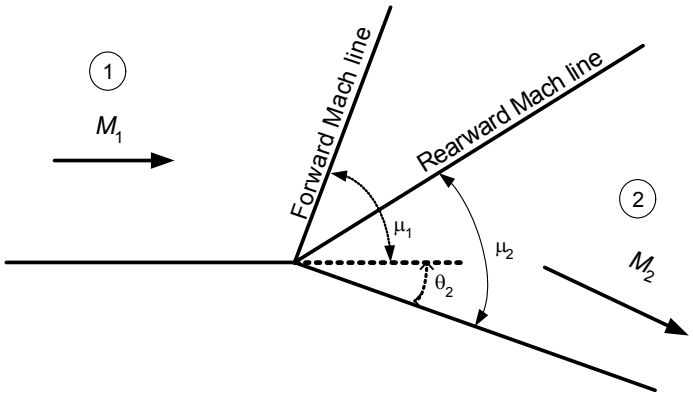

Figure 2.3 Prandtl-Meyer Expansion Wave

The equations involved in calculating the properties before and after the expansion wave are relatively simple. First $\nu(M_1)$, known as the Prandtl-Meyer function, is found by using

$$\nu(M) = \sqrt{\frac{\gamma+1}{\gamma-1}}\tan^{-1}\sqrt{\frac{\gamma+1}{\gamma-1}(M^2-1)} - \tan^{-1}\sqrt{M^2-1} \tag{9}$$

Once ν is know for M_1, the Prandtl-Meyer function corresponding to M_1 is found using

$$\nu(M_2) = \theta_2 + \nu(M_1) \tag{10}$$

The Mach number in region 2 can then be backed out using Eq. 9. Mach number corresponding to Prandtl-Meyer function is tabulated and well published. If the static pressure is known in region 1, the pressure in region 2 is calculated with

$$\frac{p_1}{p_2} = \left[\frac{1+\frac{\gamma-1}{2}M_2^2}{1+\frac{\gamma-1}{2}M_1^2}\right]^{\frac{\gamma}{\gamma-1}} \tag{11}$$

As stated earlier, expansion waves are isentropic, and therefore, total pressure remains the same in regions 1 and 2 (Anderson, 1990:134-135).

Reynolds Number

The Reynolds number is one of the most important dimensionless parameters in fluid flow. This number can be derived in physical terms by considering only the physical dimensions of those properties that determine the ratio of the inertia to the viscous forces on a volume of fluid (Kuethe and Chow, 1998:364).

Consider, for example, incompressible 2-D steady flow in a boundary layer of thickness δ; the equations governing this flow are reduced from the full Navier-Stokes equations and are shown in Eqs. (12) and (13).

$$u\frac{\partial u}{\partial x}+\upsilon\frac{\partial u}{\partial y}+\frac{1}{\rho}\frac{dp}{dx}=\nu\left(\frac{\partial^2 u}{\partial x^2}+\frac{\partial^2 u}{\partial y^2}\right) \tag{12}$$

$$u\frac{\partial \upsilon}{\partial x}+\upsilon\frac{\partial \upsilon}{\partial y}+\frac{1}{\rho}\frac{dp}{dx}=\nu\left(\frac{\partial^2 \upsilon}{\partial x^2}+\frac{\partial^2 \upsilon}{\partial y^2}\right) \tag{13}$$

The inertia forces, those on the left sides, $\upsilon\frac{\partial u}{\partial y}$, and so forth, have the dimensional form

$$\frac{V^2}{\delta}$$

where V is the freestream velocity outside the boundary layer. The viscous forces, expressed on the right side, $\nu\frac{\partial^2 u}{\partial y^2}$, and so forth, have the dimensional form

$$\frac{\nu V}{\delta^2}$$

Therefore, the ratio of the inertia forces to the viscous forces becomes

$$\mathrm{Re}_\delta=\frac{V\delta}{\nu} \tag{14}$$

termed the boundary layer Reynolds number. If Re_δ is small, the viscous forces dominate the inertia forces, and vice versa. The length δ in Eq. (14) is simply a characteristic length, and is chosen to describe a particular flow or an aspect of the flow. For flow past wings, the chord is generally chosen, although the use of Reynolds number to compare flows implies that they are geometrically similar (Kuethe and Chow, 1998:364-365).

Compressible Turbulent Jets

Figure 2.4 shows the details of the initial formation of a jet, assuming a still ambient fluid.

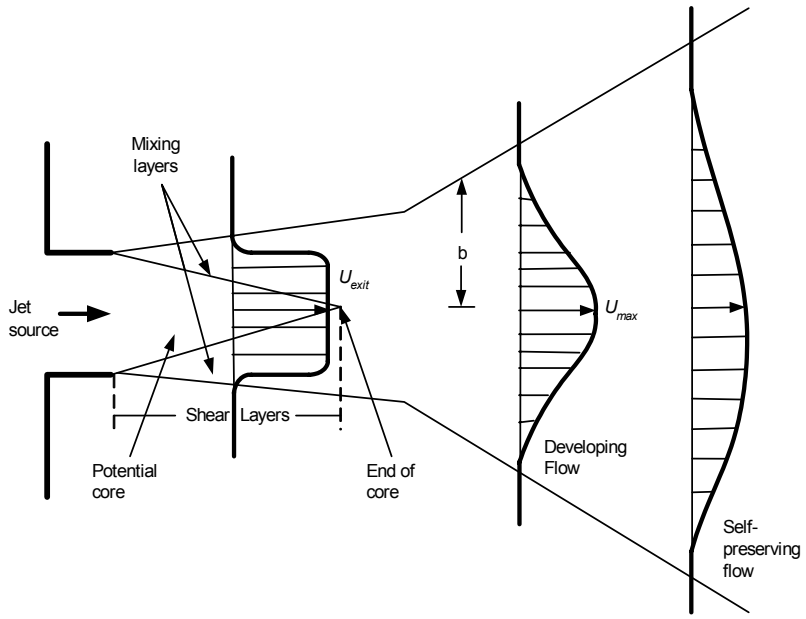

Figure 2.4 Early Development of a Turbulent Jet

Velocity profiles are shown as thick dark lines across the flow. Typically the jet issues as a nearly flat, fully developed turbulent velocity U_{exit}. Mixing or shear layers form at the lip of the exit growing between the still ambient fluid, and the nearly inviscid potential core flowing at velocity U_{exit}. The potential core vanishes quickly, at a distance of about one diameter from the exit, where the velocity profile loses its mixing-layer-flat-core shape. Down stream of the core, the flow begins to develop into the distinctive Gaussian-type shape we think of as a jet. Finally, about 20 diameters downstream of the exit, the velocity profile reaches and sustains a self preserving shape (White, 1991:471).

The jet or nozzle exit plane and external pressures are critical in analyzing the behavior of a particular turbulent jet. Shock waves or expansion fans may appear within the jet as dictated by the external environment. If the exit pressure of a nozzle is below

that of the external environment outside the exit plane, the nozzle is operating off-design and is overexpanded. If it is above the external pressure, then it is underexpanded. In the case where the exit plane pressure matches exactly with the external pressure, the nozzle is perfectly expanded (Bergren, 2002:2-6).

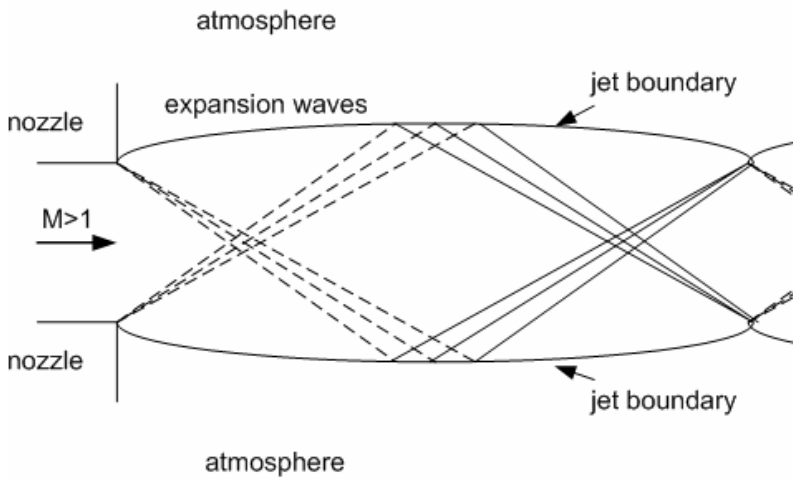

Figure 2.5 Underexpanded Jet

Figure 2.5 illustrates the actions of an underexpanded jet. As stated above, underexpansion occurs when the exit plane pressure is greater than the atmospheric pressure. This causes the jet boundary to balloon out after leaving the nozzle exit, as seen in Figure 2.5. Expansion waves occur since the flow is turning away from itself at the exit. These waves intersect each other, reflect off the jet boundary as compression waves, and intersect again to form the well understood shock diamond geometry.

Conversely, Figure 2.6 demonstrates the actions of an overexpanded jet. This occurs when the exit pressure is less than the atmospheric pressure. The jet boundary turns in at the exit causing the flow to turn into itself. Consequently, compression waves form to slow the flow down. These compression waves intersect, reflect off the boundaries as expansion waves, and form diamonds.

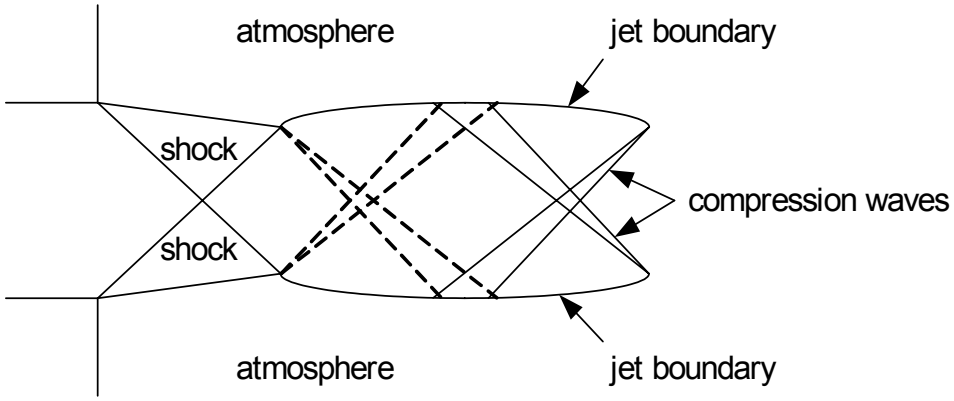

Figure 2.6 Overexpanded Jet

A nozzle array is merely a grouping of the individual nozzles discussed above. The individual jets that are formed interact with each other creating a complex flow field of interacting shear layers, compression and expansion waves, and turbulent mixing. Furthermore, as the nozzles operate at various ambient pressures, the jet interaction changes the changing flow structures (Bergren, 2002:2-9).

Figure 2.7 illustrates both the over and underexpanded cases for a nozzle array. As stated before, an overexpanded nozzle turns in at the exit plane. Therefore, little interaction occurs between the individual jets. The base region is very large and extends far downstream until complete mixing occurs. Conversely, when the nozzles are underexpanded, the plumes are much wider, and the individual jets interact almost immediately outside the exit. The base region is very small, and is isolated by the intersecting plumes. According to experiments, the nozzle base pressure has been proven to be significantly higher than the atmospheric pressure (Bjurstrom, 1984). This is consistent with Goethert's early work with non-two-dimensional nozzles. "This pressure difference is necessary since otherwise the exhaust gases in the mixing zone of the jet boundaries could not penetrate downstream into the high pressure area behind the intersections of the jets" (Goethert, 1959). As the base pressure rises, the jet can go from

being underexpanded to being overexpanded when the base pressure becomes greater than the exit pressure. After this occurs, the plumes reduce in size, exposing the base region to the atmospheric pressure.

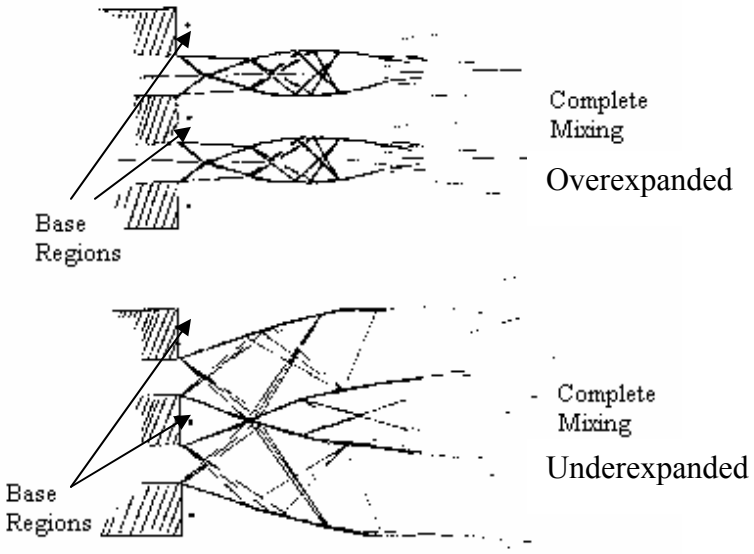

Figure 2.7 A Nozzle Cluster Operating Off-Design (Bjurstrom, 1984:24)

III. Methodology

Test Section

The test section was designed to certain criteria stated by the United States Air Force SBL IFX program office and TRW, Inc. These criteria are stated below (Bergren, 2002:2-4):

1. One quadrant or 90 deg arc of the nozzle stack and Exhaust Manifold Assembly (EMA) be modeled.
2. The flow at the nozzle exit plane be greater than Mach 1.2.
3. The ten-nozzle array consist of nine full nozzles and a half nozzle on each end.
4. The nozzles have a half angle of approximately 15 degrees.

A single quadrant of the SBL IFX is shown Figure 3.1. The nozzle array, center body, diffuser, and lasing cavity are together known as the Exhaust Manifold Assembly (EMA). These components were all modeled in the test section.

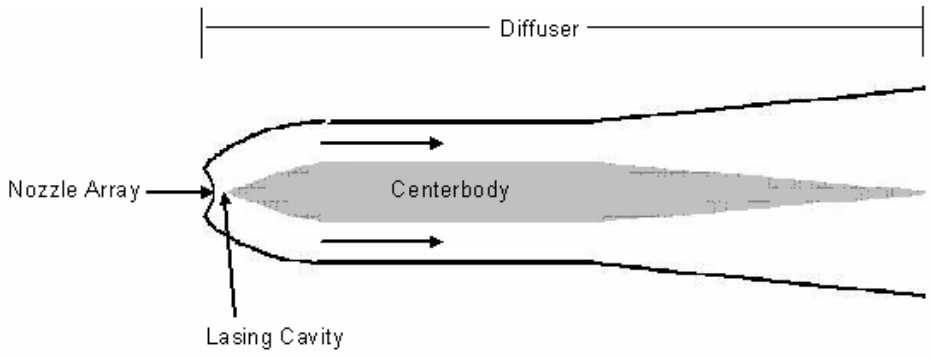

Figure 3.1 Cross-Sectional View of One Quadrant of the SBL IFX

Model Scaling.

The test section was scaled appropriately from the conceptual SBL IFX to fit the confines of the AFIT test facility. Also, cold flow (air) was used in the test section rather than the chemical fluid used in the conceptual design. The Reynolds number was the main focus in determining the scale of the model. Although the test section was scaled down in size, a close match in Reynolds number between the real and modeled flow was desired. This would make the model and the full structure dynamically similar (Sleigh, 2001). A $1/5^{th}$ scale was concluded to be appropriate for this research. This allowed the test section to be large enough to overcome viscous effects from walls, yet small enough to fit within the testing facility.

Nozzle Array.

Figure 3.2 is a computer-generated model of the $1/5^{th}$ scale nozzle array with hardware attachment points.

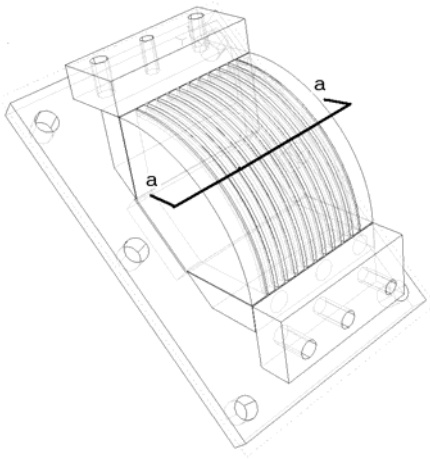

Figure 3.2 Nozzle Array Model (Bergren, 2002)

There are a few notable differences between the scaled nozzle array and the SBL IFX. One is that hydrogen was not injected into the flow as it exited the nozzles during testing.

Also air was accelerated through the nozzles instead of fluorine molecules and no lasing occurred at the nozzle exit. However, the main objective when designing the scaled nozzles was not to achieve similar fluid properties, but rather to produce similar Mach numbers at the exit plane. Using a $1/5^{th}$ scale, the cross-section of the nozzle array is shown in Figure 3.3 and a summary of the measurements is shown in Table 3.1.

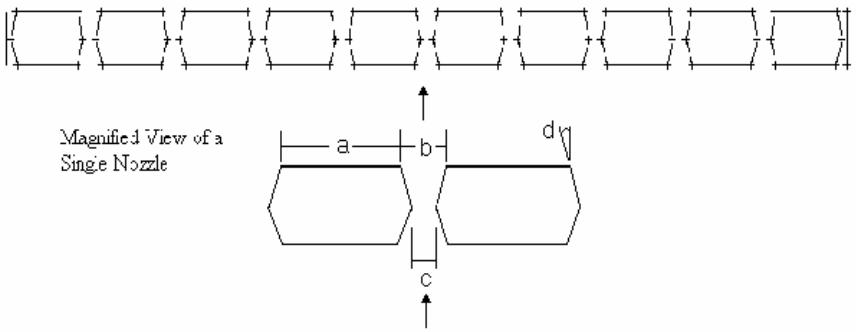

Figure 3.3 Cross-Section A-A of Nozzle Array (Bergren, 2002)

Table 3.1 Dimensions for Single Nozzle (Bergren, 2002)

	Nomenclature	*Dimension*
a	Base	4.6 mm
b	Exit Width	1.98 mm
c	Throat Width	1 mm
d	Half-Angle	15 deg

Losses were expected due to viscous effects from the nozzle walls. These effects could have been minimized by contouring the nozzle walls, but this was not feasible due to the small size. The losses due to the walls were needed in designing the exit velocity of the nozzle array. These losses were determined in preliminary tests performed by Capt Scott Bergren and described in Appendix A. From these tests, it was determined that the Mach number produced from straight walls was approximately 15% less than the Mach number

produced from contoured walls designed for isentropic expansion. Figure 3.4 is the constructed model nozzle array inside the test section.

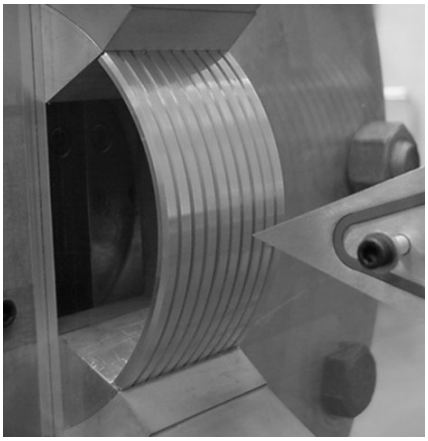

Figure 3.4 Test Section Nozzle Array

Straight nozzles were also fabricated to see the flow from the *up-down* plane. As seen above in Figure 3.4, the view of the air passing through the nozzles is going from left to right. This gives great images of shock activity around the centerbody, but not around the nozzle exit plane. Shock interactions between the individual nozzles, as illustrated earlier in Figure 2.8, cannot be seen in the *left-right* viewing plane. The *up-down* plane will give a better detailed view of these shock interactions at the nozzle exit plane. Four nozzles were fabricated for the array. The dimensions were two times larger than the circular nozzle array to give a larger image of the shock interactions. Figure 3.5 shows a picture of the straight nozzles attached to the stilling chamber and test section.

The re-scaling of the straight nozzle array will most likely have a few effects on the flow at the exit plane. The plumes of the flow exiting the nozzle array should be twice as big as the plumes exiting the circular array. The mixing length of the straight nozzle array should also be doubled. However, since the dimensions are still

proportional, the flow activity at the nozzle exit should still be relatively the same for both nozzle arrays.

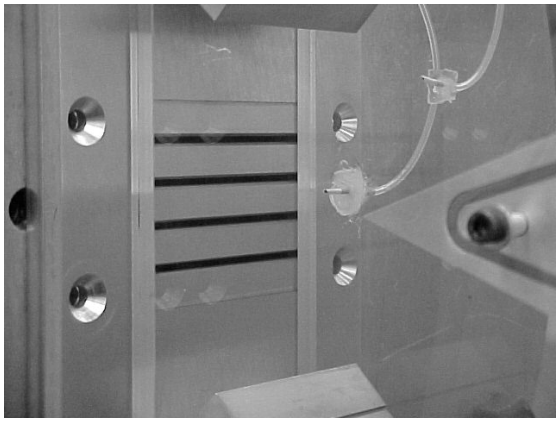

Figure 3.5 Straight Nozzle Array

Centerbody.

The centerbody was a symmetric airfoil in the center of the diffuser designed to split the oncoming radial flow into a top and bottom channel. It consisted of three pieces: the leading edge, midsection, and tail. The leading edge created a half angle of 21 deg and started 3.05 cm downstream of the nozzle exit plane. The mid-section was created using 1.91 cm thick aluminum plates and remained hollow. The tail then extended down the entire length of the diffuser with the trailing edge even with the diffuser exit plane. Figure 3.6 shows an illustration of the centerbody and its three components. O-rings were placed on both sides of the airfoil along the outer perimeter and bolts held the airfoil in place with the sidewall every 5 cm for stability.

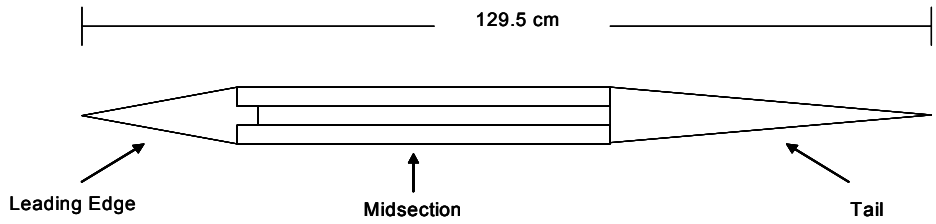

Figure 3.6 Centerbody Model

Exhaust Manifold Assembly (EMA).

The EMA is a diffuser designed to control the fluid flow. The EMA contains both the nozzle array and centerbody discussed earlier. The contour for the top and bottom of the diffuser was designed and provided by TRW. These top and bottom pieces were designed in one contoured and two straight segments to direct the radial flow exiting the nozzles to a horizontal flow while minimizing losses. The three segments can be replaced by different geometries to further investigate the optimal design for redirecting the flow. This aids in the design goal of modularity. After the scaling, the diffuser was 1.41 m in length and the height ranged from 33.3 cm at the entrance to 47 cm at the exit plane.

The majority of the sidewalls for the EMA were constructed from aluminum, but the first 76 cm was made of an optical grade Plexiglas to observe the flow characteristics within the optical cavity and around the centerbody. This was one of the main changes from the sidewalls of the test section before reconstruction. Initially, the Plexiglas only extended 30.5 cm downstream and only allowed flow visualization in the optical cavity and around the leading edge of the centerbody. With the extension of the Plexiglas, flow around the mid-section of the centerbody in addition to the optical cavity and leading edge could also be evaluated. Since no lasing occurred in the subscale model during testing, the region between the nozzle exit plane and the leading edge of the centerbody was referred to as the optical cavity rather than the lasing cavity.

Transition Structure.

The design of the transition section was critical in directing flow from the EMA to the vacuum system, while still accurately modeling the SBL IFX. Remodeling the

transition structure was a main focus of this research. Initially, the transition structure connected the exit plane of the diffuser to the vacuum system using a rectangular section measuring 76.2 cm in length which decreased in height until it mated with the vacuum line. The cross-sectional area at the beginning of the section matched the rectangular area of the diffuser exit. However, since the vacuum line was circular, the rectangular exit of the transition structure was not able to capture the entire cross-sectional area. This caused a reduction in area from the diffuser exit to the vacuum line of almost 3 to 1. A diagram of the structure before reconstruction can be seen in Figure 3.7. A photograph of the actual structure is shown in Figure 3.8

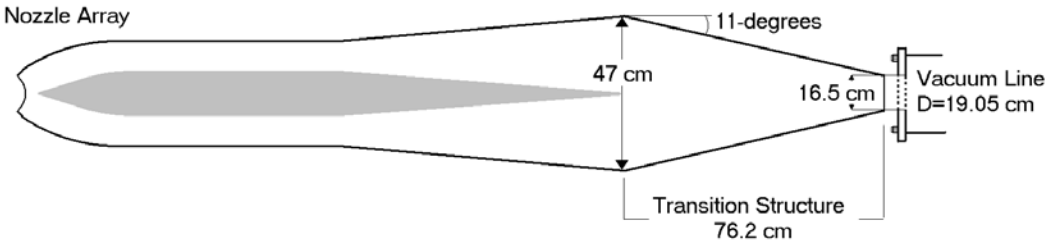

Figure 3.7 Previous Transition Structure Diagram (Bergren, 2002)

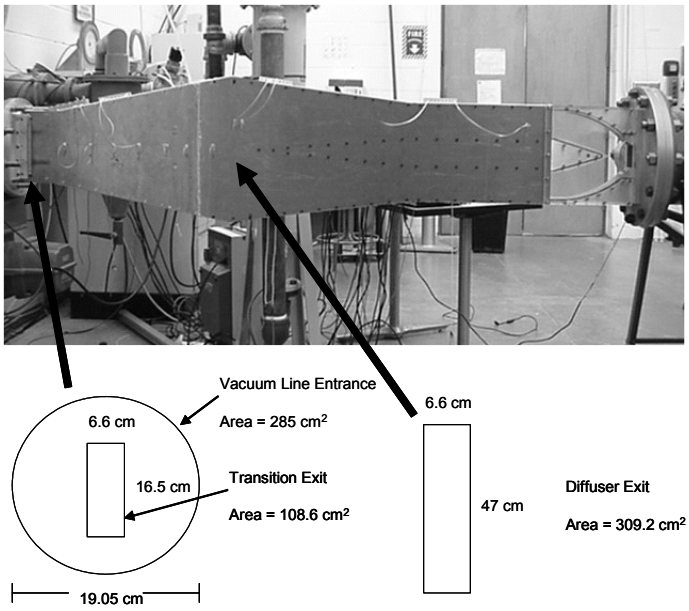

Figure 3.8 Previous Transition Structure Photograph (Bergren, 2002)

Figure 3.8 shows the reduction in area from the diffuser exit plane to the vacuum line interface. Almost two-thirds of the area of the vacuum line was lost by using a rectangular exit for the transition structure. By mating the circular vacuum line with a circular transition exit, most of the cross-sectional flow area could be recovered. Figure 3.9 shows a picture of the remodeled transition section.

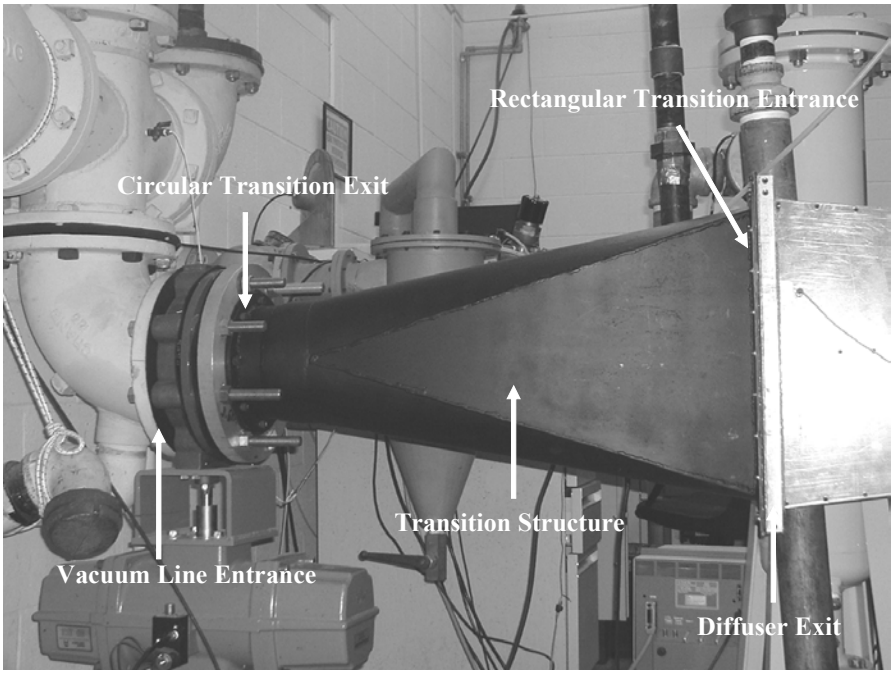

Figure 3.9 Remodeled Transition Structure Photograph

Note how the new transition structure mates to the diffuser exit in the same way that the previous one did. The only difference, however, is that instead of staying completely rectangular in shape, this new structure conforms to a circular shape as it meets the vacuum line. The vacuum line entrance and the transition structure exit area are almost nearly identical at approximately 285 cm^2. This is a large improvement over the 109 cm^2 exit area of the previous transition structure.

Wind Tunnel System

The wind tunnel system used for this research utilized a blow-down/vacuum combination which resulted in delivering a mass flow of almost 0.5 kg/s. This wind tunnel system consisted of three smaller subsystems: a compressed air system, a pressure regulating system, and ending with a vacuum system. A schematic of the entire circuit can be seen below in Figure 3.10.

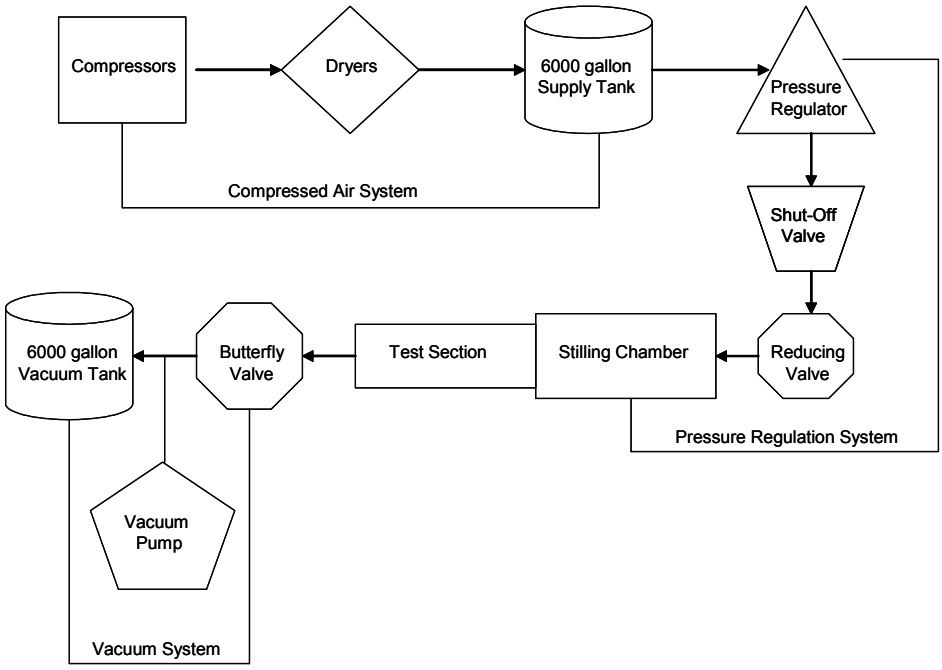

Figure 3.10 Wind Tunnel System

Compressed Air System.

The flow starts from the two Ingersoll-Rand SSR HXP 50 SE air compressors shown in Figure 3.11. These compressors provided compressed air of up to 150 psi. After exiting the compressors, the air filtered through two Ingersoll-Rand air dryers where moisture and unwanted air particles were removed. From there, a 6000 gallon

supply tank was filled and pressurized to the same pressure as the compressor air. A photograph of the air compressors can be seen in Figure 3.11.

Figure 3.11 Air Compressors

Pressure Regulation System.

After the supply tank was filled and pressurized, a diaphragm-type pressure regulator was used to reduce the supply air to a pressure of 0.62 MPa (90 psi). A 2 in, air loaded, pressure-reducing valve then reduced the pressure even further to a value set using an analog gauge controlled by the operator. The reducing valve was able to establish a set pressure reduction by balancing the pressure difference across its diaphragm. The reducing pressure range was 83 kPa – 0.9 MPa (12-133 psi). A 12 in diameter stilling chamber acted as a reservoir immediately upstream of the test section. This provided a reservoir of air at near stagnation conditions. A flow straightener was built into the downstream end of the stilling chamber to provide straight flow through the nozzles. A shut-off valve allowed the supply air to enter the test section with a switch controlled by the operator.

Vacuum System.

A 22.7 m^3 (6000 gallon) vacuum tank was evacuated by a Stokes Model 412 MBX two-stage pumping unit to provide the vacuum required to operate the wind tunnel. The pumping unit consisted of a Stokes Model 412-11 Microvac Pump and a first stage blower driven by a 10 hp and 20 hp motor, respectively. When the shut-off valve was switched on, compressed air passed through the test section to the vacuum tank at the end. This would allow the wind tunnel to operate for approximately 30 seconds for each run. Between each run, the pumping unit could evacuate the vacuum system within twenty minutes to reach a minimum pressure of approximately 3 torr (0.06 psia). A slow action pneumatic butterfly valve was positioned where the vacuum line and the downstream end of the transition section mated together. When the valve was switched to the open position, the test section was subjected to the vacuum. The length of the vacuum line from the test section to the vacuum tank was 22.25 m (73 ft) with a diameter of 19.05 cm (7.5 in). The vacuum line and its six 90-degree and two 45-degree elbows which were analyzed for loss calculations.

The final model was completed by connecting the test section to the existing wind tunnel system. A picture of the fully-assembled subscale model is shown in Figure 3.12.

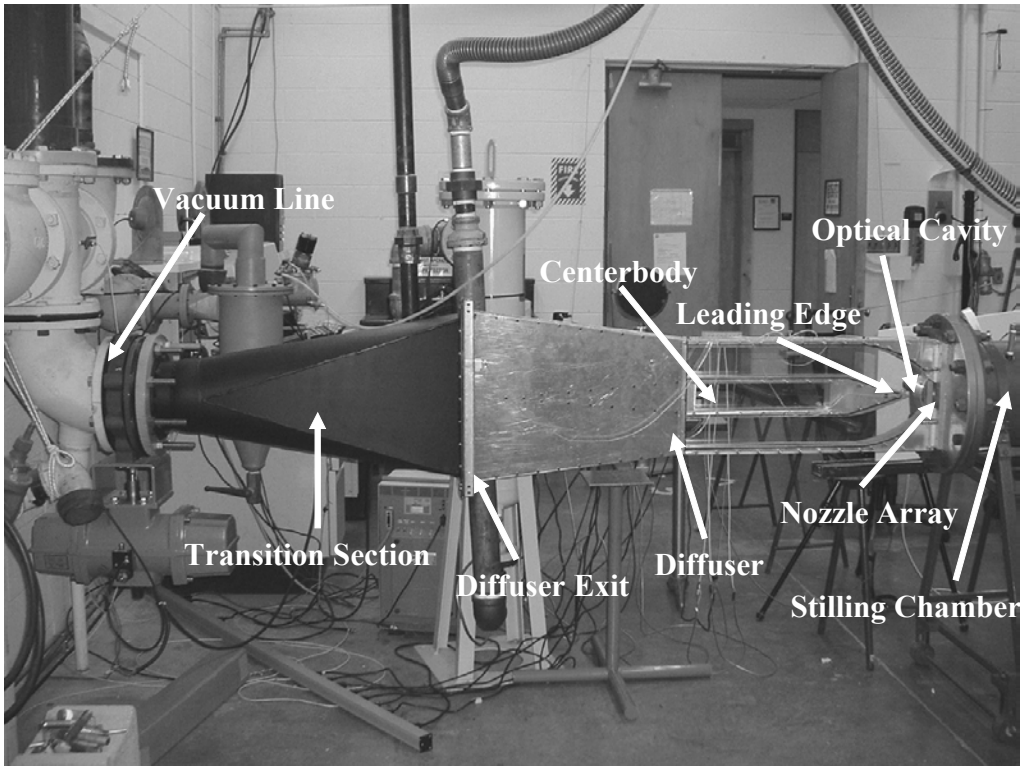

Figure 3.12 Completed Subscale SBL IFX Model with Transition Section

Data Collection

Schlieren photographs and pressure measurements were taken throughout the length of the test section to accomplish the objectives of this research. The need to capture a large number of data points required the use of a rapid data acquisition system. This provided for static pressure readings at various locations to supplement the schlieren photographs.

Pressure Transducers.

A total of seven Endevco model 8530C-50 miniature, high sensitivity piezoresistive pressure transducers (PTs) were used to collect static pressure measurements at the various locations at a frequency of 40 kHz. The seven transducers had a pressure range of 0-50 psia. The excitation voltage was 10 Vdc.

Data Acquisition System (DAS).

The Nicolet MultiPro 120 was the data acquisition system (DAS) used for this research. This multi-channel data acquisition unit was controlled by a 386 class computer running Microsoft Windows. The basics of the system included a 7 slot tower acquisition unit and four MP120 channel cards consisting of 4 channels each. The system was set to sample at a rate of 100 Hz or approximately one reading every 10 ms. All readings from the pressure transducers were fed to Endevco Model 4428A signal conditioners which filtered and amplified the signals for the DAS. These signals were then digitized by the channel cards. The system controller would then read the digitized data via a General Purpose Interface Bus for display on the computer screen using Microsoft Windows.

Schlierien Optical System.

Pictures of density gradients were obtained in the lasing cavity and parts of the diffuser using a schlieren optical system. A diagram of the setup can be seen below in Figure 3.13.

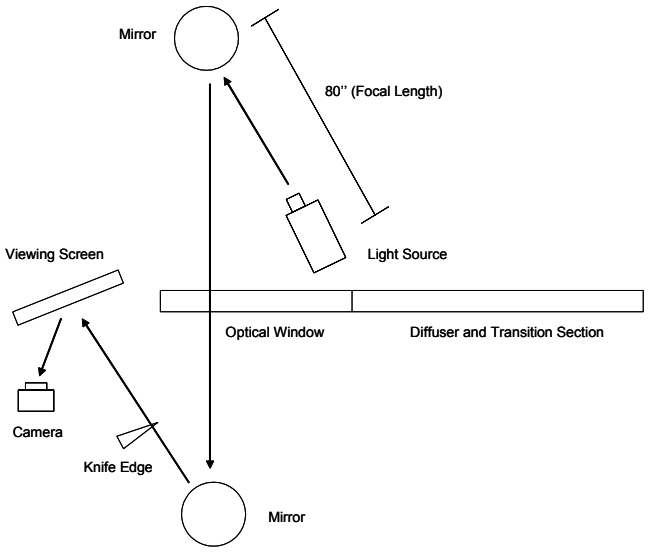

Figure 3.13 Schlieren Optical System

The light source originated from a cylindrical filament which caused the light to be slightly elongated rather than a small circular point. This slightly degraded the quality of the images shown on the viewing screen, although the images captured were still very clear. Ideally, a point light source is desired for images with the best quality. The angle between the light source and the mirrors were kept small to keep the images from distorting. As the angle between the two increases, so does the image distortion. The knife edge cut the light source vertically to obtain the density gradients. The viewing screen was a large piece of white poster board that allowed clear images of the test section. A high resolution Photron FASTCAM-X 1280PCI digital camera was used to capture the video from the viewing screen at a rate of 60 frames per second. The software provided with the camera allowed still shots to be taken from the video stream at any specified time.

Experimental Procedures

Four separate test procedures were performed to accomplish objective 2 of this research. For each procedure, a pressure transducer was located in the stilling chamber to measure stagnation pressure immediately upstream of the test section. A second transducer was located 61 cm downstream of the vacuum butterfly valve in the vacuum line. This measured the back pressure of the system.

Calibration and Uncertainty.

A portable pneumatic tester calibrated the pressure transducers at two separate pressure values. All transducers were recalibrated approximately every three days to ensure accuracy.

A detailed uncertainty analysis of the pressure readings was performed by Capt Scott Bergren in the research preceding this, and is shown in Appendix B (Bergren, 2002). The uncertainty for a single pressure measurement is 0.3 psi. This resulted from bias and precision error in both the pressure transducer and signal conditioner. This uncertainty in pressure also affected the calculations of Mach number and mass flow. These will be discussed later in Chapter 4.

Wind Tunnel Operation.

Before the test run could be started, the schlieren optical system and instrumentation had to be ready. The spark lamp was turned on and adjustments were made with the knife edge to obtain a clear and sensitive image on the viewing screen. The instrumentation was set to trigger once the test section pressure went below atmospheric pressure. Once all of this was accomplished, the wind tunnel was ready to run.

Initially all air valves were closed, and the camera capturing the schlieren images switched to record. First, the butterfly valve was opened to allow the vacuum to pull through the test section, stilling chamber, and plumbing all the way to the supply valve. This would then trigger the DAS. The system was allowed to settle for 1-2 seconds. Then the air shut-off valve was opened to release the compressed air through the system. The valve remained open until supersonic flow was no longer produced from the nozzles. The lack of gradients in the schlieren images would determine this. The air shut-off valve was then closed, followed by the butterfly valve. The DAS stopped collecting data automatically after a 30-second time lapse. The results were immediately displayed graphically on a PC monitor.

Pressure Transducer Configurations.

The same pressure transducer configurations were used for the first two procedures. In addition to the transducers in the test section, transducers were also located in the vacuum supply line and stilling chamber. Figure 3.14 shows the locations of the two transducers.

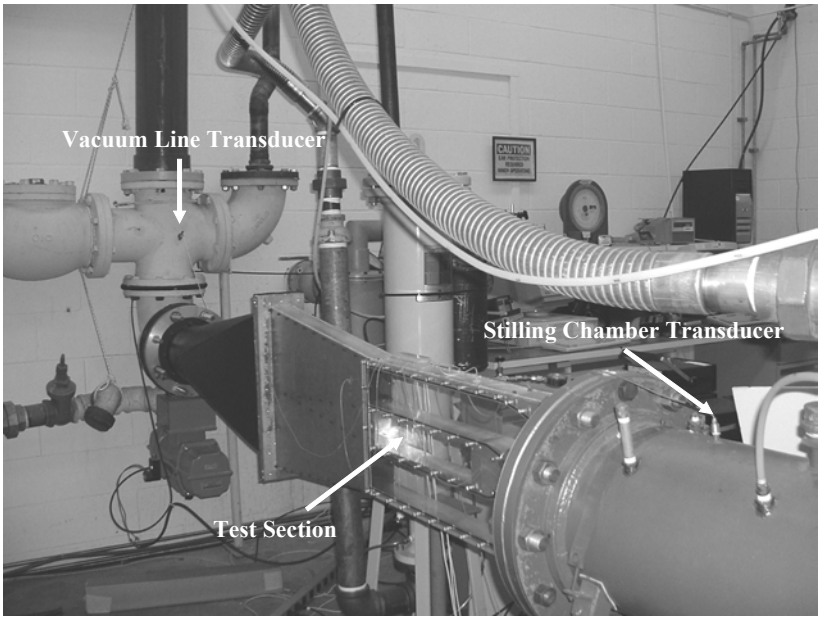

Figure 3.14 Stilling Chamber and Vacuum Supply Pressure Transducer Locations

Each pressure port in the diffuser section was drilled through the sidewall except for PT3. The port at PT3 was drilled through the top of the test section. Figure 3.15 shows a diagram of the pressure transducer locations.

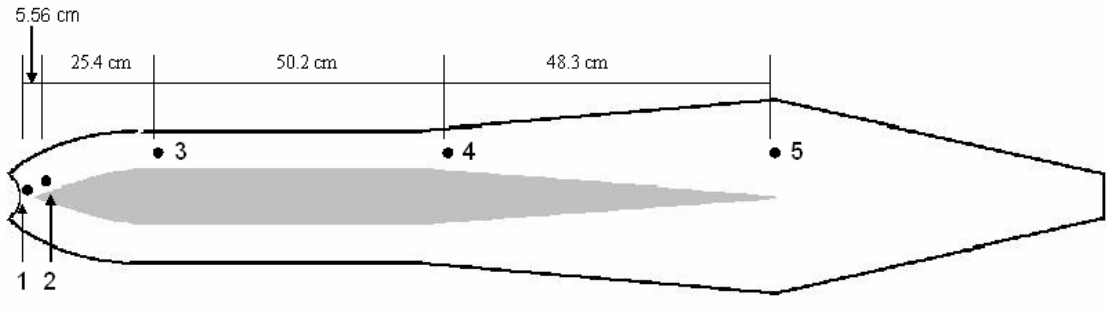

Figure 3.15 Test Section Pressure Transducer Configuration

These locations are similar to the configuration used for the previous study. The only difference is that PT1 and PT2 were added to the front of the test section. PT1 was added to collect pressure data near the nozzle exit, while PT2 collected data immediately behind the oblique shock wave. Table 3.2 provides a list of all transducers. The cross-sectional area at each location is included. The areas listed for PT2-PT4 are for only the upper half of the test section above the centerbody. This could be done since the flow was assumed to be symmetric.

Table 3.2 Cross-Sectional Areas for PT Configuration

Pressure Transducer (PT)	*Cross-Sectional Area [cm^2 (in^2)]*
1	A_1 = 100.6 (15.6)
2	A_2 = 66.8 (10.4)
3	A_3 = 59.5 (9.2)
4	A_4 = 72.9 (11.3)
5	A_5 = 150.3 (23.3)

The first two procedures used the PT configuration described above in Figure 3.15. The only difference between the two procedures was the viewing area for the schlieren optical system. Figure 3.16 illustrates the viewing areas for both procedures.

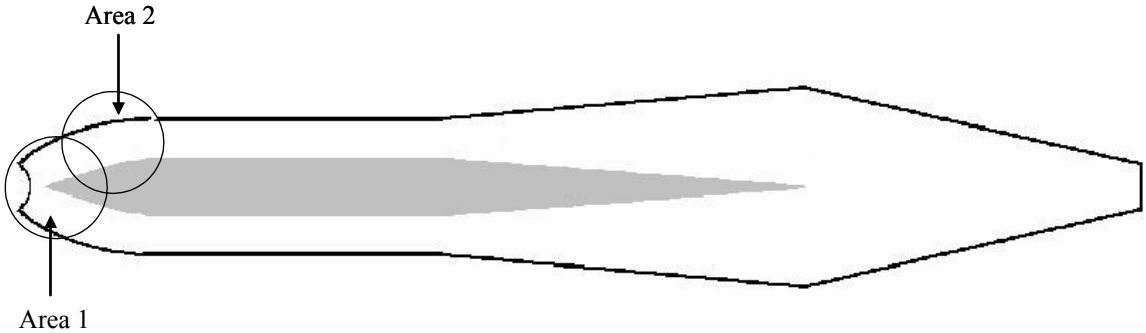

Figure 3.16 Viewing Areas for Procedures 1 and 2

Area 1 was the region downstream of the nozzle array and upstream of the centerbody. This included the expanding flow after the nozzle exit plane and the oblique shock wave that forms off the leading edge of the centerbody. Area 2 allowed visual images of the

wave reflections off the upper walls and the expanding flow around the upper level of the centerbody. These images from both areas could be combined to show a picture of flow activity for approximately the first 40 cm of the test section.

For the third and fourth procedure, the test section was removed from the stilling chamber. The straight nozzle array described earlier in this chapter was attached to the stilling chamber and test section. The butterfly valve was opened to subject the test section and stilling chamber to the vacuum. Compressed air was then released through the nozzle array and into the test section. Data was collected by a pressure transducer, PT6, 0.25 in downstream of the nozzle exit plane shown in Figure 3.17. Schlieren images were captured in Areas 1 and 2. Table 3.5 describes the separate test procedures in an experimental test matrix.

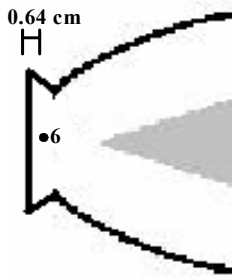

Figure 3.17 Pressure Transducer Configuration for Straight Nozzle Array

Table 3.3 Experimental Test Matrix

Test Procedure	*Viewing Area*	*Straight Nozzles*	*Pressure Transducers*
1	1	No	PT1-PT5
2	2	No	PT1-PT5
3	1	Yes	PT6
4	2	Yes	PT6

IV. Results

Pressure Measurements

The reservoir pressure shown in Figure 4.1 and the vacuum supply pressure, otherwise known as the back pressure, shown in Figure 4.2 dictated the diffuser performance during test runs.

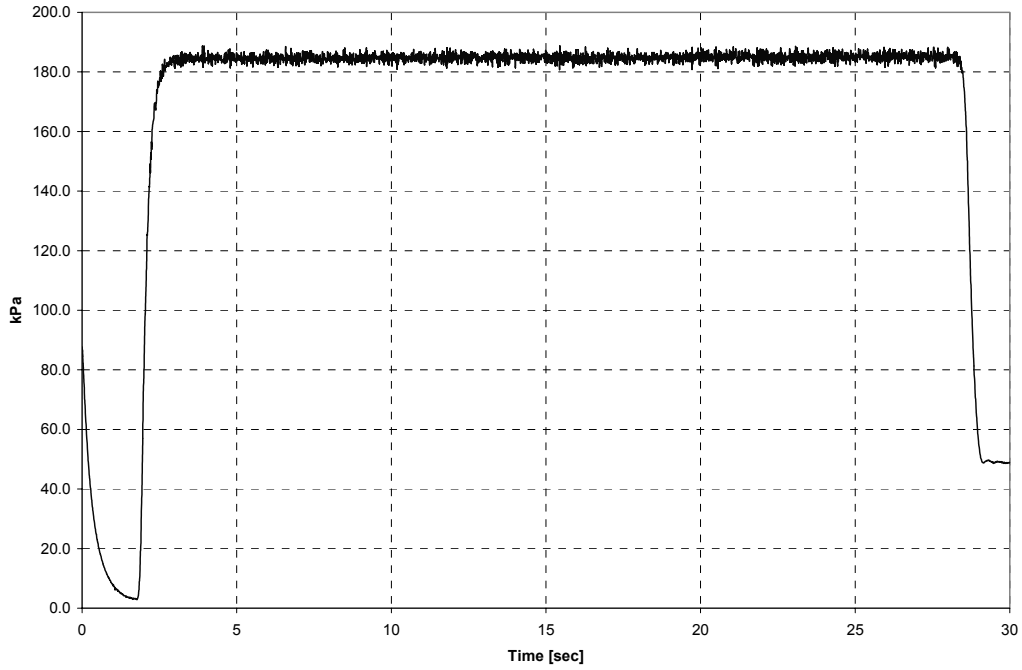

Figure 4.1 Typical Reservoir Pressure

To initiate the test run, the butterfly valve was first opened. The initial dip in Figures 4.1 and 4.2 indicated the vacuum butterfly valve opening. After the vacuum was allowed to pull on the test section for approximately one second, the compressed air was released into the test section. This is shown by the rapid increase in pressure at approximately the two-second point. After the increase, the stilling chamber stabilized its reservoir pressure and settled into a steady state until the compressed air was switched off and the butterfly valve closed at approximately 28 sec. For the particular plot shown in

Figure 4.1, the reservoir pressure reached a steady and consistent reading of about 183 kPa (26.5 psia) during the test run. As stated above in Chapter 3, there is a +/- 2 kPa (0.3 psia) uncertainty for a single pressure measurement.

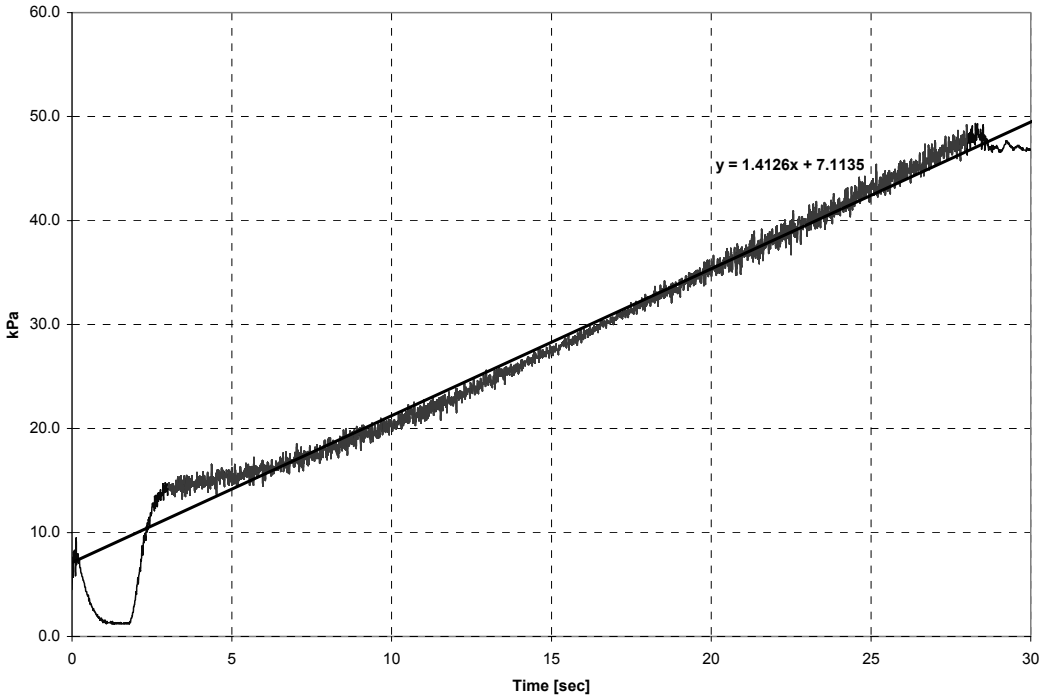

Figure 4.2 Typical Vacuum Supply Pressure

When the butterfly valve was opened, the vacuum supply pressure leveled at approximately 1.2 kPa (0.17 psia). As the compressed air entered the test section, the back pressure jumped to 13.8 kPa (2 psia). The jump in back pressure as the compressed air was released can be attributed to head loss within the vacuum system. The head loss was analytically determined to be 7.4 kPa (1.1 psia) and assumes an average velocity and density within the vacuum lines. The detailed calculations of the head loss can be found in Appendix C.

While the compressed air ran through the test section, the back pressure increased in a near linear fashion. This was indicative of a steady mass flow. As seen in Figure

4.2, the linear regression line fit shows the back pressure rose at a rate of 1413 Pa/s (0.2 psia/s). Analytically, the back pressure was predicted to rise at a rate of 1759 Pa/s (0.26 psi/s). The rate the back pressure rises is dependent on the reservoir pressure. The higher the reservoir pressure, the higher the rate of change. These calculations can be seen in Appendix D.

The mass flow rate was calculated using Eq. (1) from Chapter 3. This calculation was applied at the throat of the nozzle where the flow was assumed to be choked and the Mach number equal to one. The results are shown below in Figure 4.3.

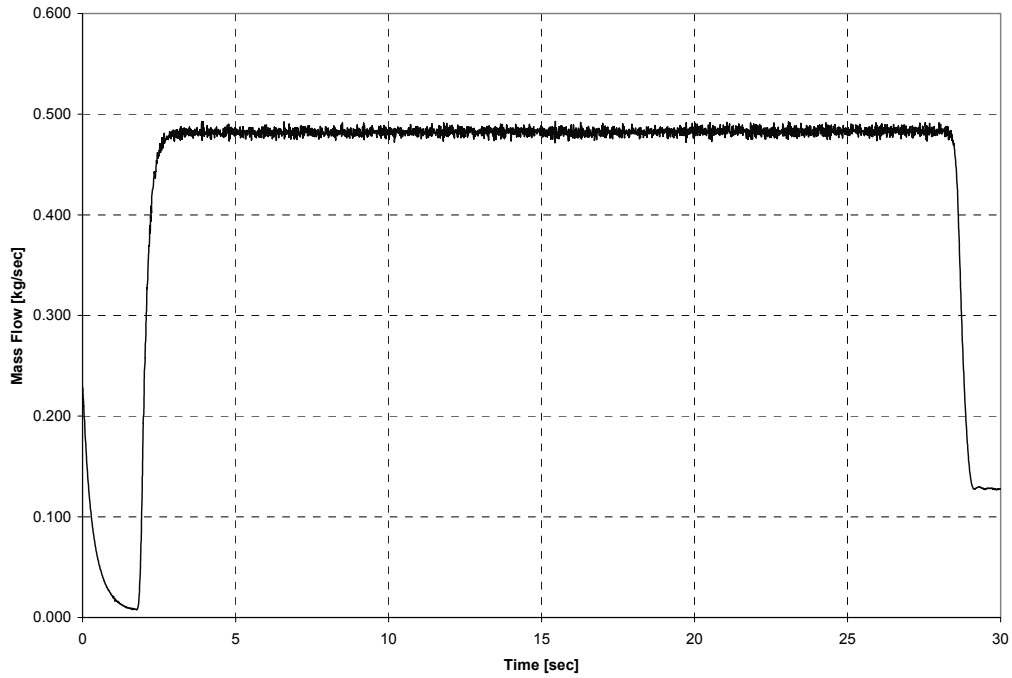

Figure 4.3 Typical Mass Flow Rate

The mass flow rates shown above correspond to the reservoir pressure readings displayed in Figure 4.1. The reservoir temperature was assumed to be at room temperature (290 K) and constant. Since the mass flow calculations are directly dependent on pressure and temperature, the shape of the plot displayed in Figure 4.3 matches exactly with that of Figure 4.1. For this particular test run, the mass flow is

constant at a rate of 0.48 kg/s. According to Capt Scott Bergren, the maximum error for a single mass flow calculation was determined to be +/- 4.7 g/s and the calculations are shown in Appendix B.

Pressure data was collected to determine Mach number at various locations throughout the diffuser. Figuer 4.4 shows the static pressure measurements for PT1, PT2, and PT3.

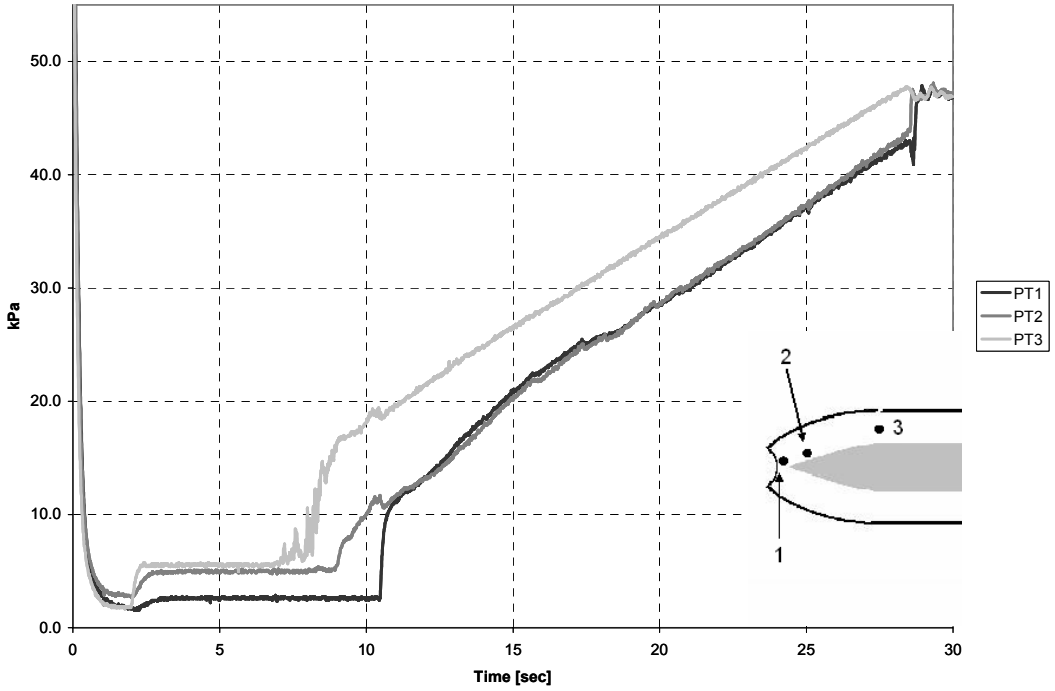

Figure 4.4 Static Pressures for PT1, PT2, and PT3

The Mach number was calculated for PT1, PT2, and PT3 using the static pressure measurements from Figure 4.4 and cross-sectional area as stated in Eq. (2) from Chapter 3. These results are shown in Figure 4.5.

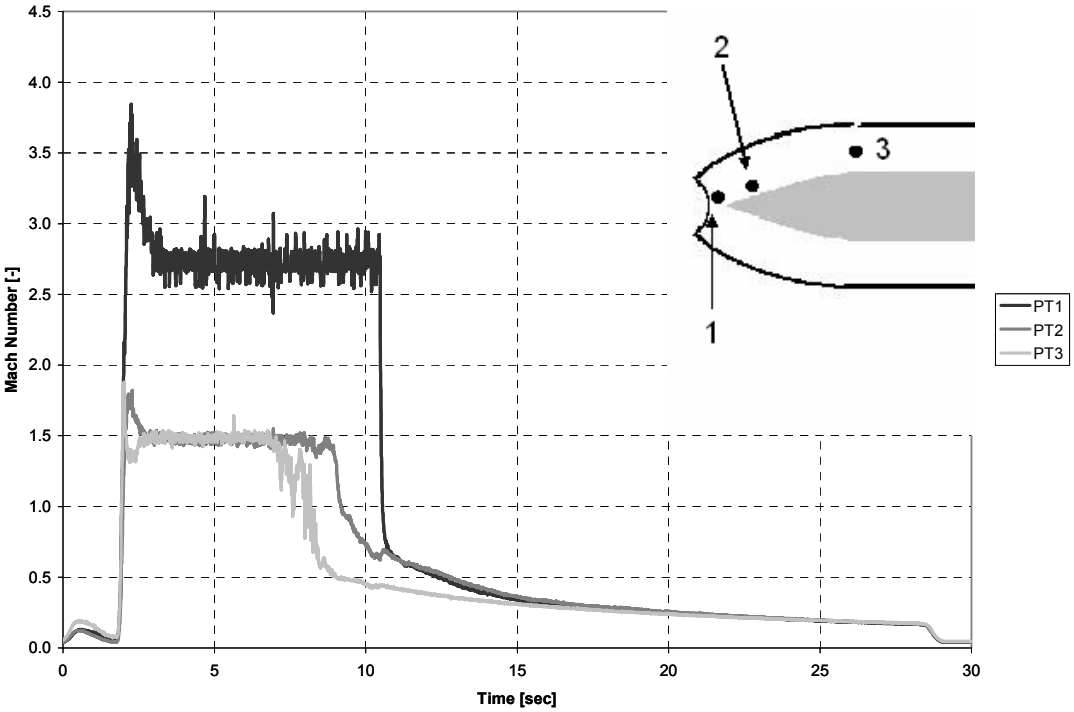

Figure 4.5 Mach Numbers for PT1, PT2, and PT3

As seen in Appendix B, the max error for a single Mach number calculation is +/- 0.1. This was the case for Mach number calculations at every PT location. The highest velocities were shown to be at PT1 directly aft of the nozzle exit plane. This is expected since the air has not yet had a chance to be diffused. As the air travels down the length of the diffuser it is slowed. This is seen in the difference in velocities from PT1 to PT2. At PT1, the Mach number peaks at approximately 3.8 and then levels at 2.7. Although Figure 4.5 shows a peak of Mach 3.8, the flow never actually reaches this velocity. The peak is due to the method in calculating Mach number. The Mach number calculated above is based on the mass flow rate from the stilling chamber. In the calculations, once the compressed air is turned on, it is assumed that the mass flow is constant along the entire test section. However, in reality, it takes the air a small amount of time to reach each pressure transducer. Therefore, immediately after the compressed air is switched

on, the pressure readings are very low at the transducers and the mass flow rate is high in the reservoir. Eq. (2) shows that a high mass flow rate combined with a low pressure will result in a higher than expected Mach number.

Once the Mach number levels, the flow reaches a steady state, as shown in Figure 4.5. Both Mach numbers at PT2 and PT3 level at approximately 1.5. The decrease in Mach number from PT1 to PT2 and PT3 is caused by an oblique shock formed at the leading edge of the centerbody. PT1 is in front of the shock, while the other two are behind it. Mach number decreases across the shock, as shown in Figure 4.5. This will be explained further in detail when the schlieren results are reported. The Mach number remains at this level until the flow at each location becomes subsonic due to the rising back pressure. Since PT3 is the closest transducer to the vacuum supply, the rising back pressure causes it to be the first transducer to record subsonic speeds. This is shown in Figure 4.5at approximately 7 seconds. PT2 follows at about 9 seconds, and finally PT1 records subsonic speeds at about 11 seconds. Since the compressed air was released at about two seconds, PT1 holds its "steady state" for approximately 9 seconds.

The temperature used to calculate Mach number at all three points was found using an iterative procedure. First, an initial guess was used for the local temperature at each transducer. The guessed local temperature was then compared to the total temperature in the stilling chamber, assumed to be room temperature (290 K), to obtain a static-to-total temperature ratio. Using tabulated isentropic relationship tables, the corresponding Mach number was found (Kuethe and Chow, 1998). This value was then compared to the calculated value from Eq. (2). If the two Mach numbers did not match, the initial guess for the local temperature was adjusted until the two numbers converged.

The local temperatures for PT1, PT2, and PT3 converged at 107, 202, and 201 K respectively. The increase in temperature from PT1 to PT2 and PT3 is expected. As the distance down the diffuser increases, the Mach number will decrease. Since Mach number is inversely related to temperature, this would indicate that temperature should increase.

To validate the results at PT1, the Mach number was also calculated using the isentropic pressure relationship shown in Eq. (3). Total pressure from the stilling chamber was compared to the static pressure read by PT1. Figure 4.6 shows the comparison of the calculated Mach number using both Eqs. (2) and (3).

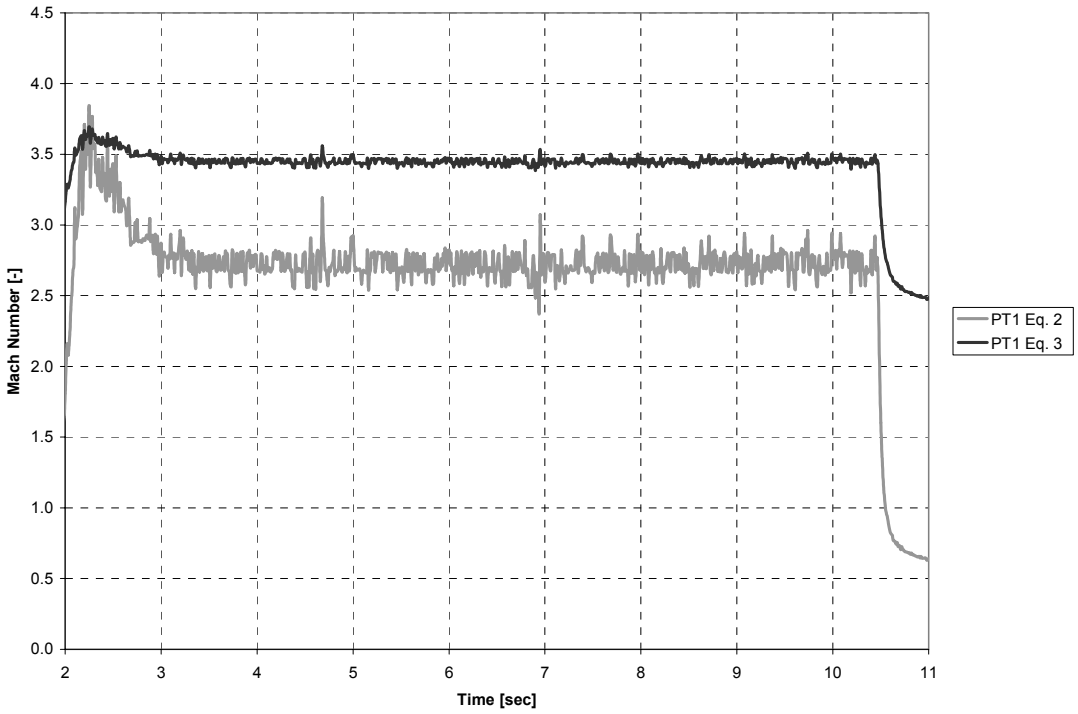

Figure 4.6 Comparison of Calculated Mach Number at PT1 Using Eqs. (2) & (3)

Since the steady state portion of the run is the focus of interest, only t = 2-11 seconds is shown in Figure 4.6. During the steady state portion of the test run, Mach number calculated using Eq. 2 is approximately 20% less than the Mach number from Eq.

3. The Mach number from Eq. 3 only relies on the total pressure recorded in the stilling chamber and the static pressure recorded by PT1. Eq. 2 takes into account both the cross-sectional area and static temperature at PT1. The difference between the two calculations indicates that iterating on temperature to determine Mach number from Eq. (2) allows for more uncertainty. Also, the cross-sectional area measured at PT1 could be slightly off, contributing to the difference.

The calculated results do take into account the losses due to the uncontoured walls of the nozzles. Using Eq. (3) and assuming isentropic flow (contoured walls), the Mach number at the nozzle exit plane was calculated to be approximately 3.4 during the steady state period. Capt Scott Bergren, through experimental procedures shown in Appendix A, determined that the losses through the nozzles were approximately 15%. This would make the actual Mach number at PT1 approximately 2.9. This is within 5% of the calculated Mach number shown in Figure 4.5

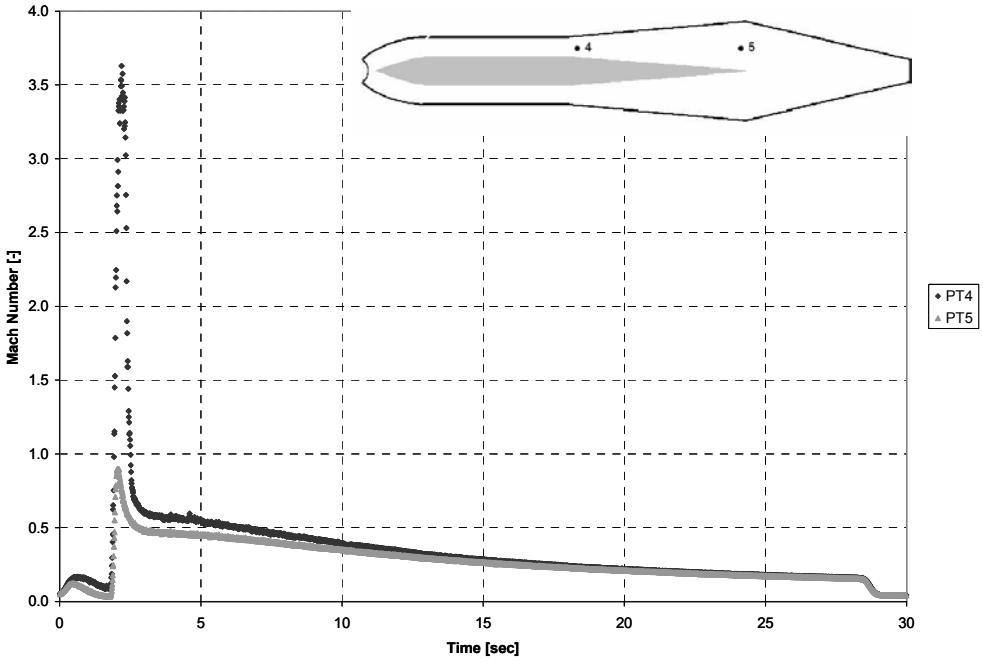

Figure 4.7 Mach Numbers for PT4 and PT5

For PT4 and PT5, both transducers in Figure 4.7 show subsonic speeds immediately after startup. The Mach numbers for the two locations are almost identical throughout the run. PT4 is higher at initial startup, but then converges to the values of PT5 around the 10 second point. As stated earlier, the peak Mach number of 3.6 at PT4 resulted from the method of calculation rather than the actual fluid velocity. Since the two transducers are located towards the end of the diffuser, subsonic speeds are expected at these locations. The temperatures at these locations were also found using the iteration procedure discussed earlier. The static temperatures for both PT4 and PT5 were found to be 260 and 272 K, respectively.

Schlieren Images

The schlieren optical system was used to capture video images. After the video was captured, computer software allowed still images to be seen at any point in time. As explained earlier in Chapter 3, two different areas were viewed. Since the images in Area 1 and 2 had to be captured in two different test runs, matching the reservoir pressure was the key to obtaining matching results. This would insure that the flow for both procedures were nearly identical. The reservoir pressures for the two runs were within 0.2 psi of each other. Since the two pressures were very close, the shock waves from the two areas matched very well. An image of the two areas combined at t = 5s can be seen in Figure 4.8.

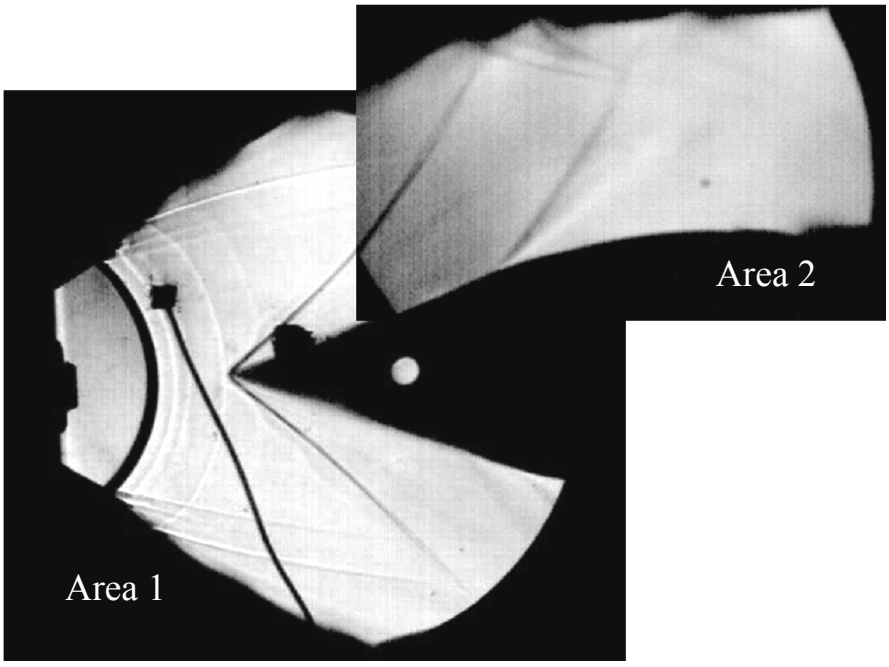

Figure 4.8 Combined Schlieren Image of Areas 1 and 2 at Time = 5.0s

Although there is no way to match the times of Areas 1 and 2 exactly, the two images are both taken during the steady state period. Therefore, the shock formations are not significantly changing with time and the images could be combined.

For many of the following figures, the view area is circled in the upper right hand corner. Because the light in the schlieren system only reflects off one mirror after traveling through the test section, the images projected on the viewing screen are reversed and upside-down when compared to the actual flow. The images have been modified to show the actual flow direction as seen in Figure 4.9.

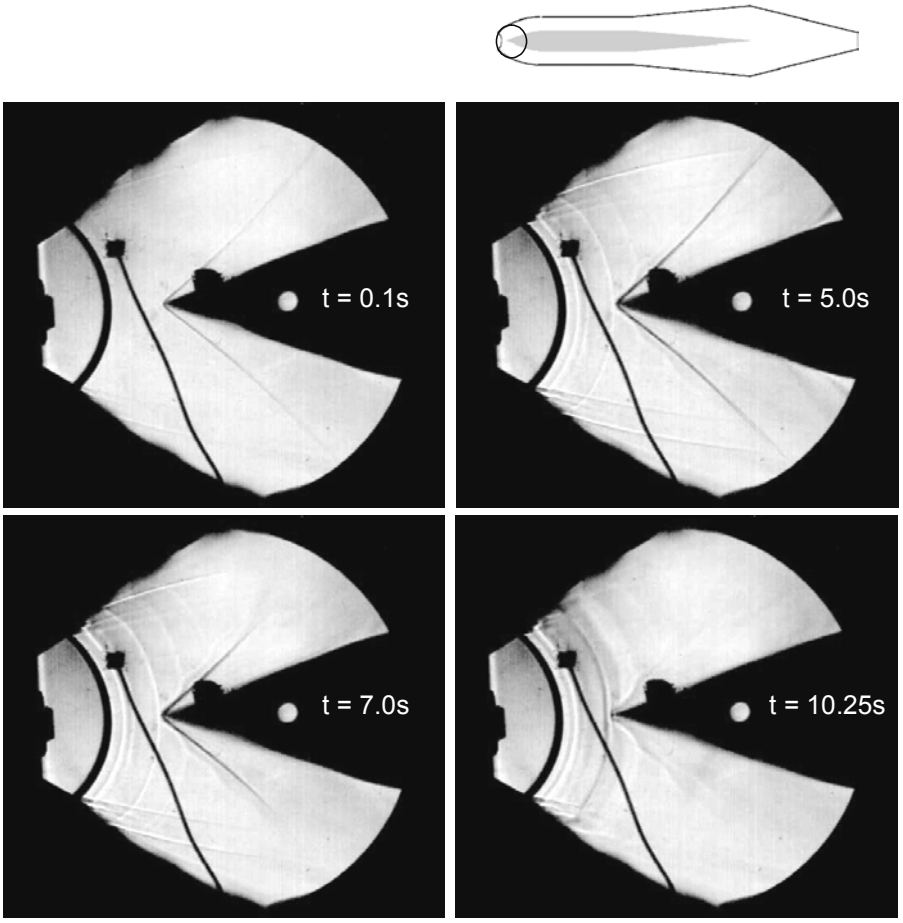

Figure 4.9 Schlieren Images of Oblique Shock Wave Motion in Area 1

When the compressed air is released into the test section, an oblique shock wave immediately forms off the leading edge of the centerbody, as shown at t = 0.1s in Figure 4.9. This shock wave holds until approximately seven seconds after the compressed air

was released. At this point, the back pressure has started to push the shock wave towards the nozzle array. This process continues until the shock wave detaches from the leading edge and becomes perpendicular to the radial flow at t = 10.25s. This gives a total steady state time of over 10 sec. In previous results produced by Capt Scott Bergren, a steady state time of only 0.2 sec was achieved. This run time extension is mostly due to the remodeling of the transition structure. Enlargements of the photographs shown in Figure 4.9 can be seen in Appendix E.

The measured shock wave angle at t = 5.0s and the wedge half-angle dictate that the flow at the leading edge of the centerbody was traveling at approximately 2.8. This is only slightly higher than the velocity at PT1 during its steady state shown previously in Figure 4.5. This is possibly due to the +/- 0.1 calculation error in Mach number. Since the nozzle exit plane Mach number was designed to be 2.2, the multiple jets must be underexpanded at the exit, and further expansion occurs after the nozzle exit plane to accelerate the fluid to Mach 2.7 before the transducer at PT1.

Using the schlieren image from t = 5.0, the pressure at PT2 was analytically calculated and compared to the experimental results below in Figure 4.10. The analytical calculations can be seen in detail in Appendix F.

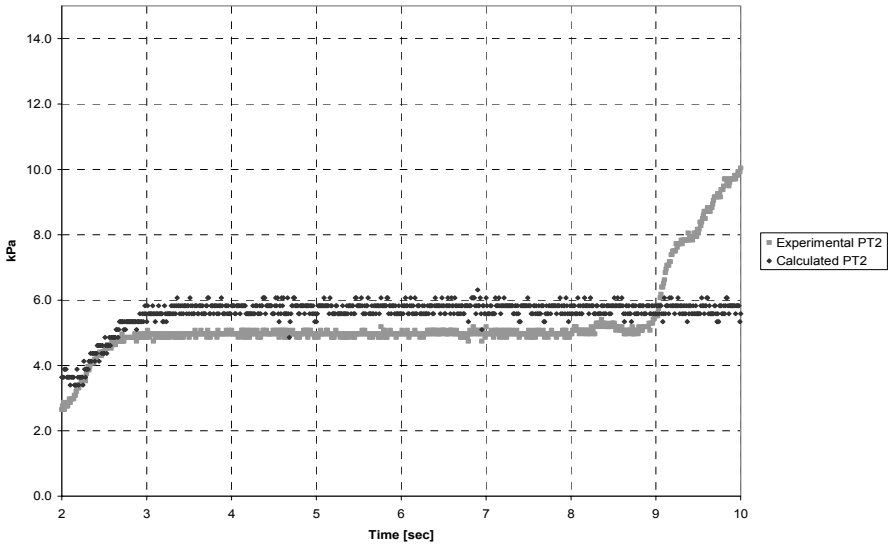

Figure 4.10 Comparison of Experimental and Calculated Pressure at PT2

Figure 4.10 only displays the time from 2-10 seconds since the steady state period is the only time of interest. The calculated pressure is slightly higher than the experimental pressure by approximately 15%. The shock wave angle and turning angle used to calculate PT2 was 40 deg and 11 deg, respectively. The calculated pressures in Figure 4.10 were based on pressure readings from PT1 immediately after the nozzle exit plane. The light radial lines in the optical cavity indicate expansion still occurs past PT1 which would cause static pressure in front of the leading edge of the centerbody to drop slightly from PT1. Since no transducer is located immediately forward of the leading edge, PT1 was used to analytically determine readings at PT2. This is most likely the cause for the higher calculated pressures in Figure 4.10. The analytical calculations can be seen Appendix F.

The Reynolds number (Re) at the leading edge was calculated to be approximately 2.8×10^5. The characteristic length used for calculating Re was the distance from the center of curvature of the nozzle array to the leading edge of the centerbody (0.105 m). Velocity and static temperature at the leading edge were

calculated using the schlieren images in Figure 4.9. Density was calculated using ideal gas properties and pressure measurements from PT1. The purpose of calculating Reynolds number was to determine if similarity was achieved. TRW determined the Reynolds number at the leading edge of the wedge to be approximately 1.8×10^4 through computational results. Therefore, the subscale model is an order of magnitude higher than the numerical results found by TRW. The reservoir pressure was reduced to try and match the Reynolds numbers, but the lowest pressure achievable was 59 kPa (8.5 psia). Since the regulating system operated only on guage pressure, the diaphragm was not able to regulate under atmospheric conditions. Using this pressure the Reynolds number was 1.9×10^5.

The reduction in reservoir pressure may have reduced the Reynolds number, but the Mach number remained the same at each location for all test runs. The reason for this is demonstrated in Eqs. (1) and (2) shown earlier in Chapter 2.

$$\dot{m} = \frac{p_0 A^*}{\sqrt{T_0}} \sqrt{\frac{\gamma}{R}\left(\frac{2}{\gamma+1}\right)^{(\gamma+1)/(\gamma-1)}} \tag{1}$$

$$M = \frac{\dot{m} RT}{pAa} \tag{2}$$

As the reservoir pressure is reduced, mass flow and static pressure also decrease. If both of these values lower proportionally, no net change in Mach number will occur, as shown in Eq. (2).

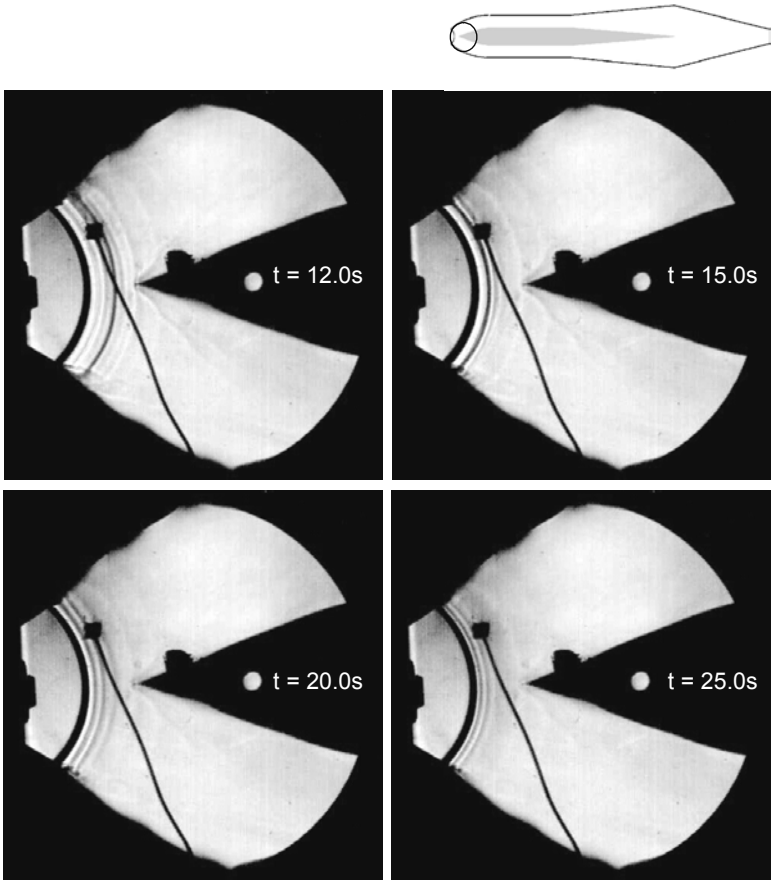

Figure 4.11 Schlieren Images of Normal Shock Wave Motion in Area 1

As shown in Figure 4.8, the shock becomes normal to the flow and detaches from the leading edge at t = 10.25s. Figure 4.11 provides a sequence of images immediately following the ones shown in Figure 4.9. The normal shock travels upstream towards the nozzles after detaching from the leading edge. At 15 seconds, it has almost reached the nozzle exit. At 20 seconds, multiple shock waves form to rapidly slow down the flow in order to meet the rising back pressure behind the shocks. Lastly, at 25 seconds, the waves move closer together and stand immediately downstream of the nozzle exit plane. The images in both Figure 4.9 and 4.11 show that the flow is symmetric.

The distance the lines are observed downstream of the nozzles can indicate whether the flow in underexpanded or overexpanded. Immediately after the compressed

air is released into the test section, the nozzles are underexpanded. This is shown by the flow continuously expanding after the exit plane in Figure 4.8 and 4.9. At t = 25s in Figure 4.11, the back pressure has driven the normal shock wave almost completely to the nozzle exit. For an overexpanded nozzle, the shock diamond pattern should extend no more than 5-6 nozzle widths from the exit plane (Bjurstrom, 1984). Since the shock is within this range, it can be assumed that the nozzles become overexpanded at approximately 25 seconds. Therefore, for each test run, the nozzles start underexpanded until the back pressure rises high enough to drive the shock forward and make the nozzles overexpanded at approximately 25 seconds.

The amount of time for the nozzles to switch from underexpanded to overexpanded is dependent on the reservoir's operating pressure. A higher reservoir pressure will cause the back pressure to rise at a higher rate, therefore, the higher the reservoir pressure is, the faster the nozzles will become overexpanded.

Schlieren photographs were also taken immediately downstream of Area 1 to get the full picture of the shock activity throughout the diffuser. These pictures can be seen in Figure 4.12.

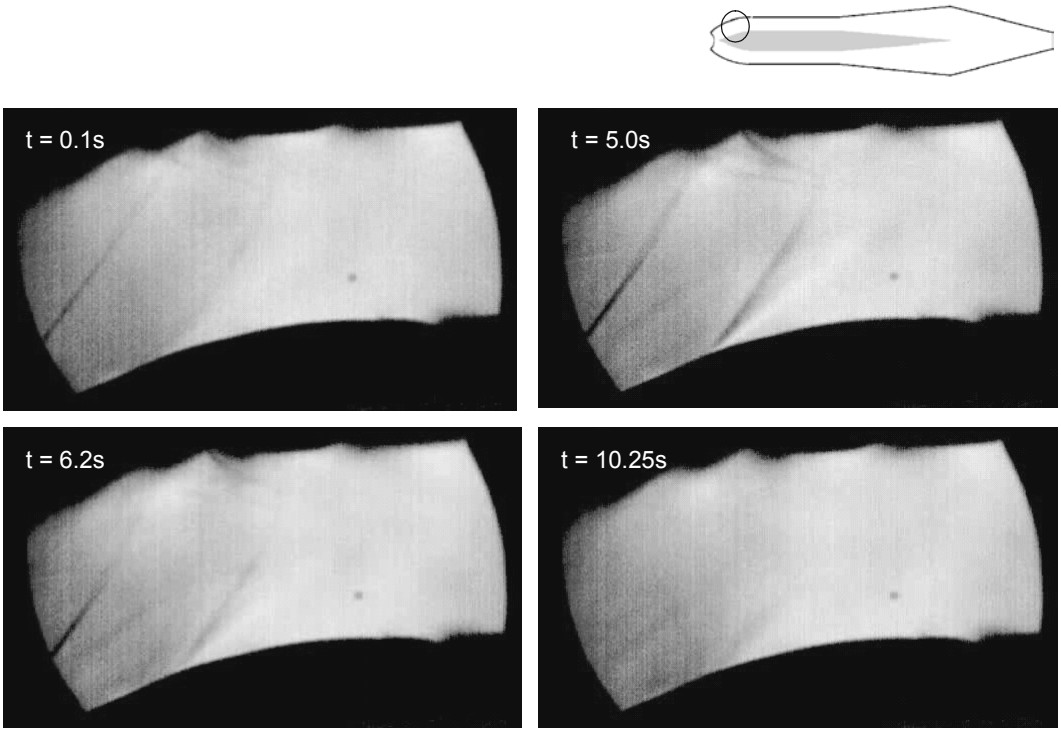

Figure 4.12 Schlieren Images of Oblique Shock Wave Motion in Area 2

As in Area 1, an oblique shock is seen immediately after startup. The reflection of the oblique shock is seen off the outer wall. Since the shock appears to travel all the way to the wall, this is an indication that there is no separated flow along the wall. The shock and reflections hold until approximately 6 seconds, where the shock wave starts to move forward. This is slightly ahead of the time when the oblique shock wave attached to the centerbody moved forward in Area 1. This is to be expected since Area 2 is farther downstream and closer to the diffuser exit. At t = 10.25s, the shock waves are completely pushed upstream, and the flow in area 2 is now subsonic. Enlarged images of the ones shown in Figure 4.12 can be seen in Appendix G.

One advantage to the view in area 2 is the picture of the second shock wave attached to the centerbody. In Figure 4.9, it is barely seen at the far right side at t = 5.0s. In Figure 4.12, it is well defined and seen in its entirety.

Since there is no turning angle to cause the shock, an in depth analysis is needed. PT2 shows that during the steady state period, the Mach number is approximately 1.5. During the same time, the Figure 4.5 indicates that the Mach number at PT3 is also approximately 1.5. This is shown in Figure 4.13.

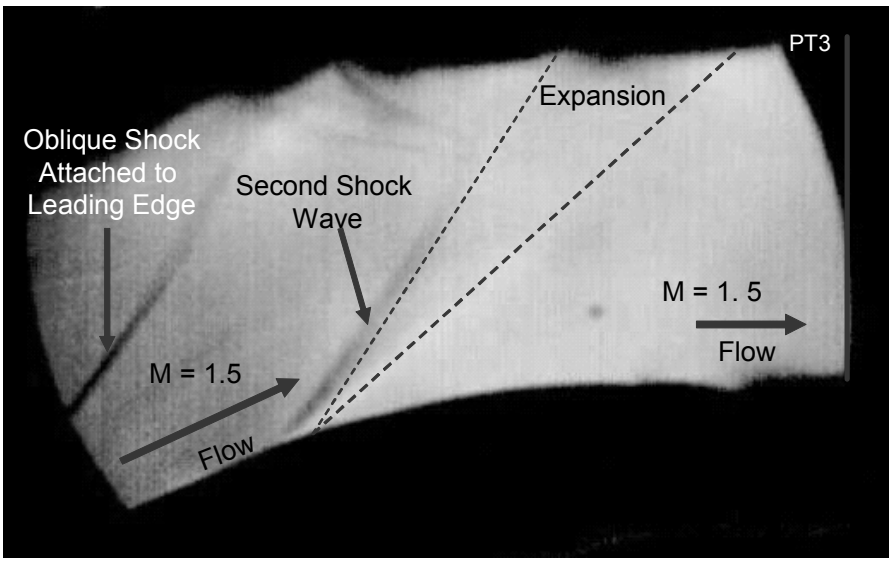

Figure 4.13 Detailed Schlieren Image of Area 2 at Time = 5.0s

After the flow passes the first oblique shock wave, it must turn 21 deg to become straight and flow along the mid-section of the centerbody. According to expansion wave theory, a flow at Mach 1.5 and turning 21 deg should accelerate to Mach 2.2 after the turn. However, Figure 4.13 shows the flow at only Mach 1.5. This was measured at the location shown for PT3. Since the back pressure is constantly rising during the test run, flow at PT3 does not exceed Mach 1.5. This is the reason for the second shock wave indicated where shown in Figure 4.13. Flow must expand around a corner, and in turn, accelerate according to theory. However, in order for the flow to accelerate to 1.5, the

original flow before turning must be approximately 1.1. Therefore, an oblique shock wave must form before the turn to decelerate the flow after the initial shock from Mach 1.5 to 1.1. The flow then expands around the corner, as shown in Figure 4.13, and accelerates to the measured Mach 1.5 at PT3. Therefore, it is evident that the flow conditions downstream dictate the activity upstream rather than the other way around.

Optical Cavity Analysis

The optical cavity shown in viewing area 1 is the most important area for flow analysis in the diffuser. As stated earlier in Chapter 1, the quality of the laser beam is highly dependent on the flow characteristics within the lasing cavity. Therefore, a detailed analysis of all shock activity within the optical cavity is needed. Figure 4.14 identifies expansion fans in the optical cavity during the steady state period.

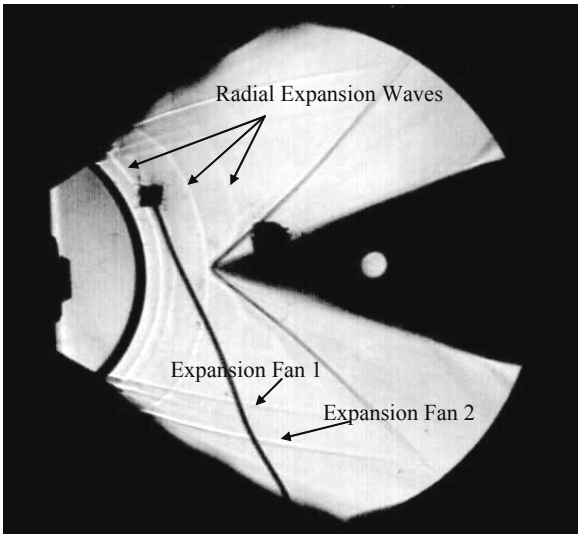

Figure 4.14 Horizontal Expansion Fans in Optical Cavity

As seen above, there are a couple of light horizontal lines which run through the top and bottom of the cavity. The first line originates at the very top and bottom of the nozzle

array. The upper and lower outer walls at the nozzle exit are not exactly perpendicular to the nozzle exit plane. It actually "flares out" a little as seen in Figure 4.15.

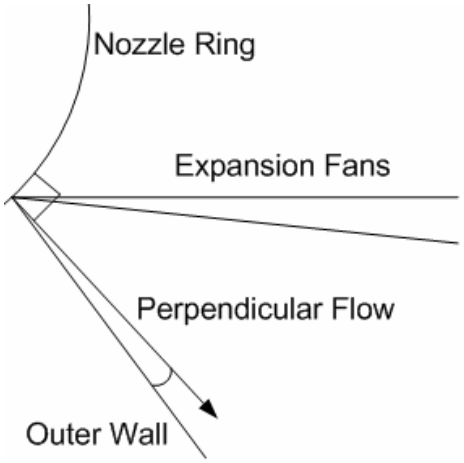

Figure 4.15 Orientation of Outer Wall at Nozzle Exit

The sketch above is an exaggerated view to show how the outer wall is "flared out." Since the flow exiting the nozzle array must turn to travel parallel to the outer wall, an expansion wave must occur. This explains the first light horizontal line leaving the top and bottom of the nozzle array.

The second expansion fan runs horizontally from the outer wall to the oblique shock wave. This expansion wave is immediately followed by a shock wave. These two actions are caused by caused by a small step in the outer wall illustrated in Figure 4.16.

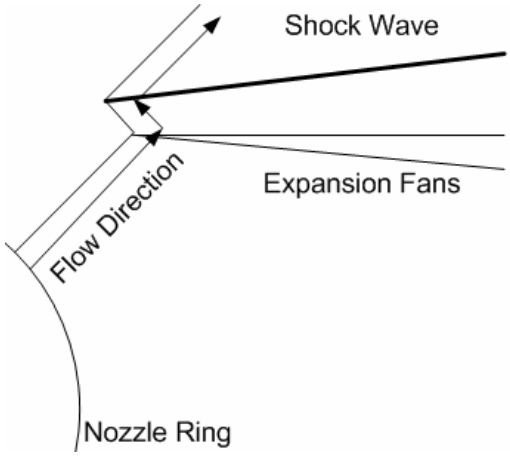

Figure 4.16 Sketch of Outer Wall Step

This step was in the TRW design of the diffuser and therefore, was put into the design of the test section. Since the flow must turn twice during this step, an expansion fan is formed during the first turn, and then a shock wave is formed to bring the flow back parallel to the wall. The expansion fan is evident in the very light shaded line running from the step to the oblique shock wave. If the line is observed closely, a black line can be seen outlining the expansion fan on the outer side. This is an indication of the shock wave which brings the flow back parallel to the wall.

The expansion of flow from the nozzle exit plane to the leading edge can be seen in the faint radial lines in the optical cavity normal to the flow, as pointed out in Figure 4.14. These are most likely the intersecting expansion waves from each individual jet. Due to the orientation of the light source and the nozzle array, the expansion waves and shock diamonds discussed in Chapter 2 cannot be seen in the schlieren images. A diagram of the light source orientation through the nozzle exit plane can be seen in Figure 4.17. The intersecting expansion and compression waves are the largest gradients in the image and appear as lines perpendicular to the flow as seen in Figure 4.11 and 4.15. The light lines indicate expansion, while the dark ones show compression shocks.

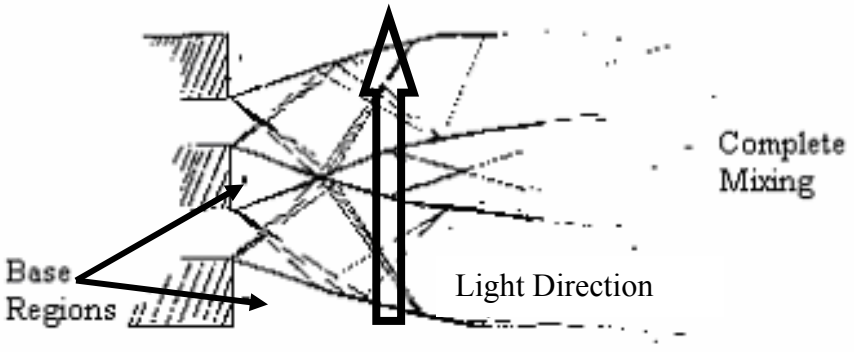

Figure 4.17 Schlieren Light Source Orientation

When the flow reaches the second horizontal expansion fan shown in Figure 4.14, the flow turns with the step, but the shock wave turns the flow back to travel parallel to the outer wall. Th is is indicated in Figure 4.16. The flow continues to turn into itself as it follows the outer wall. Since the outer wall is straightening the flow, the oblique shock attached to the wedge must "bow" towards the nozzles slow down the flow. This is the reason for the curve in the oblique shock wave near the outer walls.

Comparison to CFD Results

Comparing the experimental results to the CFD results obtained by TRW was part of the second objective of this research. Figure 4.18 displays the image in Figure 4.8 along side a Mach line contour plot obtained numerically by TRW.

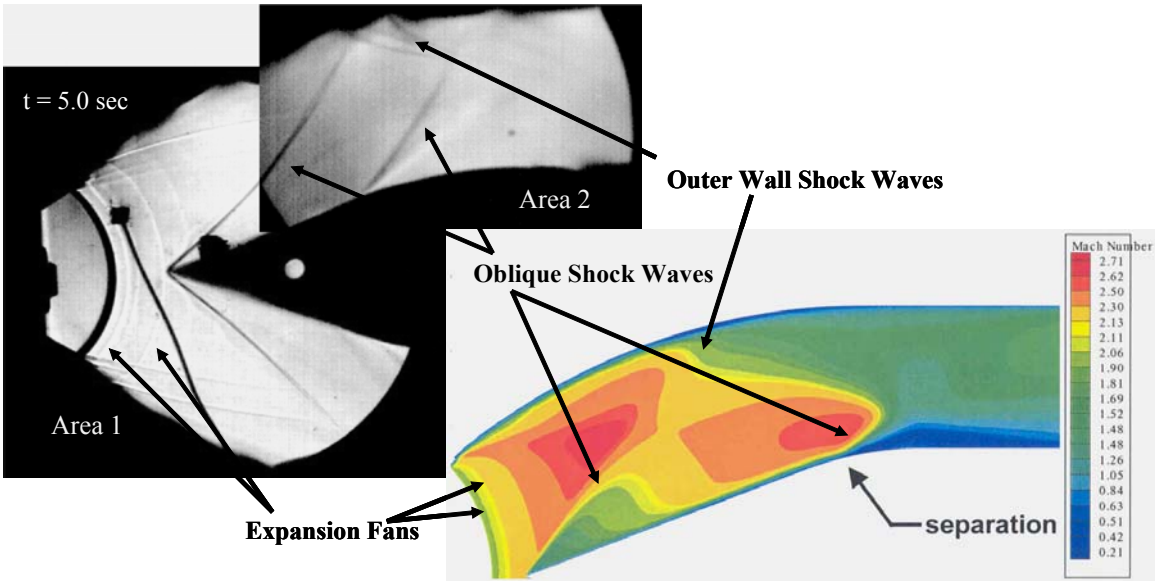

Figure 4.18 Comparison of Experimental and CFD Results in Areas 1 & 2

The first thing to notice is that both results contain an oblique shock wave that forms off the leading edge of the centerbody. However, the angle for the shock wave in the CFD results is slightly higher. This results in a smaller Mach number of approximately 2.3 at the leading edge for the numerical results. As mentioned earlier, the

angle for the experimental results indicates a Mach number of approximately 2.8 at the leading edge of the centerbody. This difference is probably due to the slight variations in geometry between the numerical and subscale model. For instance, the distance of the centerbody from the nozzle exit plane should be 1.2 in according to the conceptual TRW design. However, the actual distance in the subscale mode is approximately 1.32 in. This can contribute to the difference in Mach number between the two results.

Another difference is the experimental shock wave bends towards the nozzles as it gets closer to the outer wall, while the numerical shock wave bends towards the diffuser exit. This can attributed to the rising back pressure of the experimental results. In the numerical results shown above, a constant back pressure of 7 torr (0.15 psi) was used. As stated earlier in Chapter 3, the vacuum was able to evacuate the air in the test section down to approximately 3 torr (0.06 psi). However, after the xompressed air was released into the system, the head loss jumped the pressure up to 13.8 kPa (2 psi) within approximately 0.1 sec. Therefore, the rising back pressure for the experiment started out much higher than the constant back pressure for the numerical results. Since the back pressure was much less for the numerical results, and was constant throughout the test run, the shock wave was able to bed towards the diffuser exit rather than towards the nozzle array.

A second oblique shock wave is also seen in both results. Both of these shock waves occur where the centerbody turns to become straight and parallel with the outer wall. The difference between the two shock waves, however, is that an expansion fan occurs immediately after the experimental shock wave, while separation occurs behind the numerical shock wave. No evidence of separation is seen in the experimental results.

The Mach number behind the second oblique shock wave matches the Mach number of the experimental results. Both show a velocity of approximately Mach 1.5 in this region.

Other points of interest between the two results are the radial expansion fans seen in both results. During the steady state portion of the run, radial expansion fans are present in the optical cavity for both results as identified in Figure 4.18. Since the cross-sectional area is increasing between the nozzle exit plane and the leading edge of the centerbody, the supersonic flow expands as it exits the nozzle array. This is similar for both results.

Finally, both results show shock waves coming off the outer walls as identified in Figure 4.18. These waves are caused by reflections of the oblique shock wave attached to the leading edge of the centerbody, and the outer wall straightening the flow. The shock waves from the experimental results start farther downstream than the ones shown in the CFD results. This is due to the faster Mach number at the leading edge for the experimental tests. Since the flow at the leading edge is faster for the experimental tests, the shock wave coming of the leading edge has a smaller angle. This will cause the reflection off the outer wall from this wave to occur farther downstream.

Most of the differences between the two results can be attributed to the rising back pressure during experimental testing, and slight differences in measurements between the numerical and subscale model. Despite these small differences, the images shown in Figure 4.18 indicate that the two flows are very similar.

Straight Nozzle Analysis

Straight nozzles were analyzed to see the flow at an angle 90 deg to that shown with the circular nozzle array. Figure 4.19 shows a time sequence of the flow exiting the straight nozzles into Area 1.

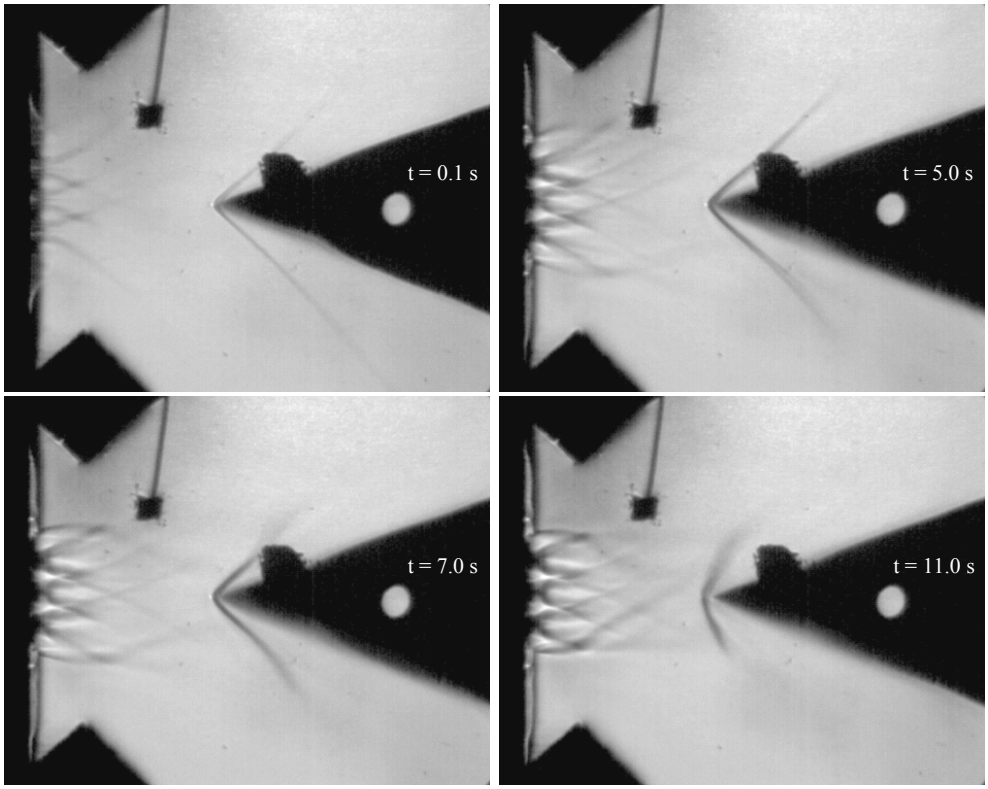

Figure 4.19 Straight Nozzle Flow in Area 1

The reservoir pressure for these test runs was nearly identical to that of the circular nozzle tests. They matched to within 0.3 psi. This insured that the pressure ratio between the nozzle opening and nozzle exit were the same for both procedures. Immediately after the compressed air was released, an oblique shock wave similar to Figure 4.9 attached to the leading edge of the centerbody. Using the angles of the wedge and the shock wave, the Mach number was calculated to be approximately 2.8 at the leading edge. This is identical to the Mach number calculated in Figure 4.9. Enlarged images from Figure 4.19 can be seen in Appendix H.

The flow followed a similar pattern to that of Figure 4.9. Initially, the nozzles were underexpanded at the nozzle exit plane and an oblique shock wave attached to the leading edge of the centerbody. During the steady state portion of the test run, the oblique shock wave held its form and the individual jets of the nozzle array were fully interacting with each other. Notice how the oblique shock wave bowed forward toward the nozzle array as it got closer to the outer wall. This is similar to Figure 4.8. At approximately 7 sec, the back pressure starts pushing the shock wave forward toward the leading edge of the centerbody. At approximately 11.0 sec the oblique shock wave was nearly detached from the leading edge. The shock wave totally detaches from the leading edge at approximately 13 seconds.

These actions and the times of their occurrence are slightly longer than those shown in Figure 4.9. This can be attributed to the differing mass flows between the two procedures. With the circular array, the ten nozzles have a cross sectional area of 11 cm^2 at the throats. The straight nozzle array only has a total throat area of 5.27 cm^2. Since the straight array has almost half the area of the circular array, the mass flow rate is reduced by nearly a half. During the steady state period for both procedures, the mass flow rates for the straight and circular array were 0.23 kg/s and 0.48 kg/s, respectively. Since the mass flow is less with the straight array, it takes longer for the vacuum tank to fill, and the back pressure does not rise as quickly. Therefore, it takes longer for the back pressure to cause subsonic flow upstream for the straight nozzle array.

Figure 4.19 also shows how the flow at the nozzle exit changes with time. At t = 0.1 and 5 sec, it can be seen that the nozzles are underexpanded since the flow expands outward towards the outer walls. As time progresses, the plumes become smaller and the

flow does not expand outward as far. This is seen at t = 7 sec. At t = 11 sec, the flow exits the nozzles in an almost straight line. This confirms that the nozzles are underexpanded after startup, but transition to overexpanded as the back pressure rises.

Schlieren images were also captured from the straight nozzle array in Area 2. Figure 4.20 shows a sequence of the flow activity in this area. Enlarged images can be seen in Appendix I.

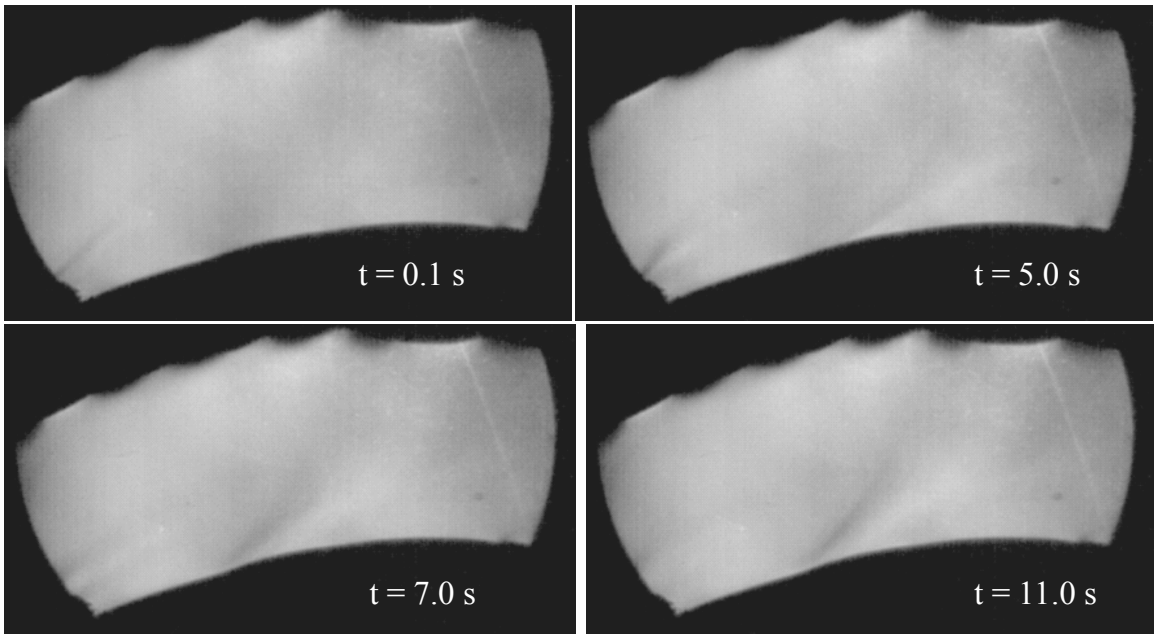

Figure 4.20 Straight Nozzle Flow in Area 2

Figure 4.20 shows similar flow activity to Figure 4.12. During the steady state for both nozzle arrays, an oblique shock comes off the centerbody just before the turn, and an expansion wave occurs immediately after it. Figure 4.21 shows this in more detail. One difference, however, is the length of time the second oblique shock stays in place. Even after 11 s, the oblique shock is still present. This again is due to the lower mass flow rate of the straight nozzle array. The back pressure has not raised high enough to cause subsonic flow at this location yet.

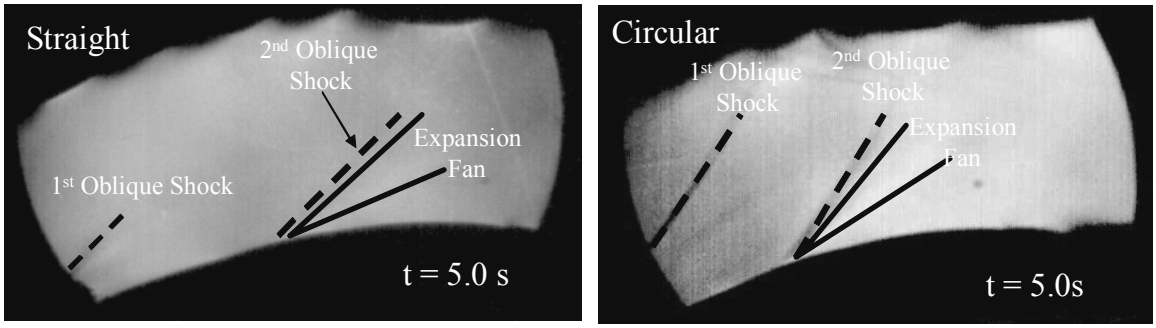

Figure 4.21 Shock Activity in Area 2 at T = 5.0 sec

As stated earlier, the shock activity in Area 2 are very similar for both the circular and straight nozzle arrays. Figure 4.21 identifies the oblique shock waves and expansion fans for both arrays, since it can be a little hard to see in the previous images. The second oblique shock wave seems to occur at approximately the same location and the expansion wave occurs immediately downstream of the shock wave for both arrays. This gives a good indication of flow similarity between the two nozzle arrays.

The image from Figure 4.19 at t = 5.0 s can be shown with Figure 4.9 at t = 5.0 s to compare the steady state flow interactions from two different angles at almost identical times. Figure 4.22 identifies expansion wave intersections in the optical cavity from the two different angles. The approximate distances between intersections are also shown.

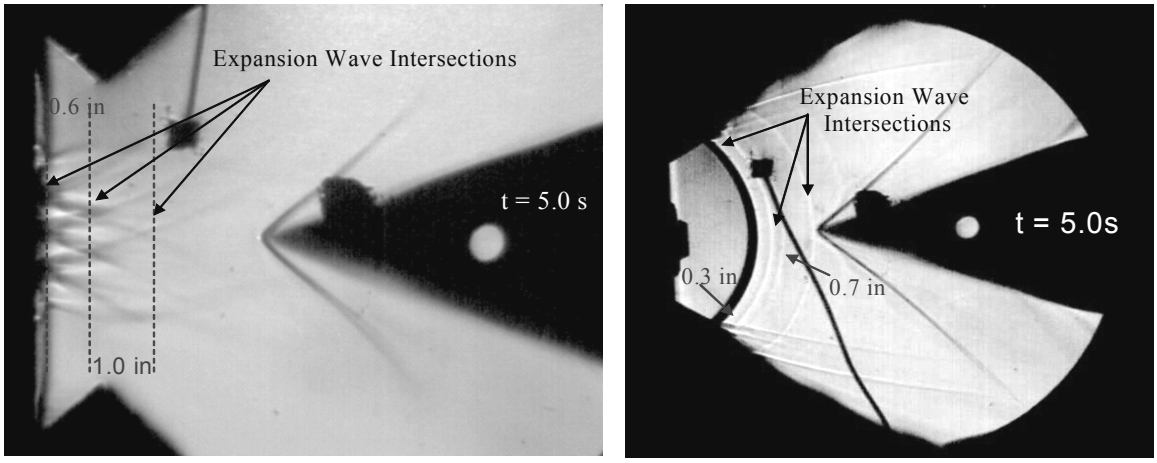

Figure 4.22 Expansion Wave Intersections in Optical Cavity at T = 5.0 sec

The flow seen in the first image of Figure 4.22 compares with the underexpanded nozzle cluster drawing shown in Figure 2.8. The first intersections seen are immediately after the nozzle exit plane. This is barely seen in the circular array image. Two more wave intersections can be seen downstream in the optical cavity before reaching the leading edge of the centerbody. In the straight nozzle array, the second intersection occurs approximately 0.6 in downstream of the nozzle exit, while the circular array shows a distance of approximately 0.3 in. The third intersection is almost 1 in downstream of the second intersection for the straight array compared to 0.7 in for the circular array. The distances for the straight nozzle array are approximately double the distances for the circular nozzle array. This can be attributed to the fact that the dimensions of the straight nozzle array are twice as big as the circular array.

PT6 pressure data was collected approximately 0.25 in downstream of the nozzle exit plane. The data was used to determine Mach number at this location. Figure 4.23 and 4.24 display the static pressure and the Mach number, respectively, at PT6.

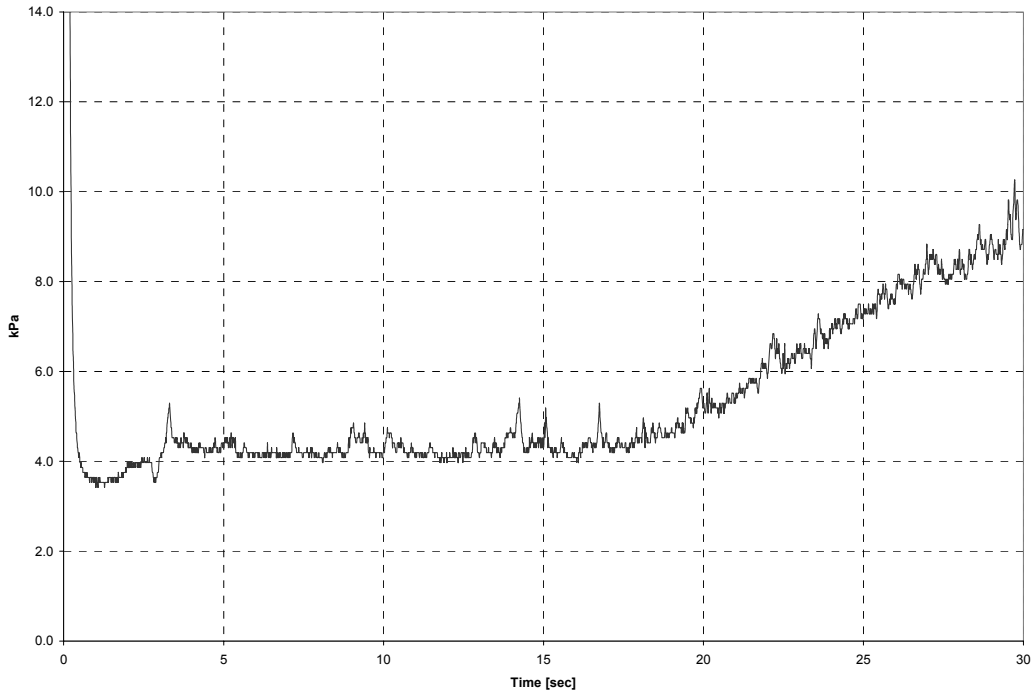

Figure 4.23 Static Pressures for PT6

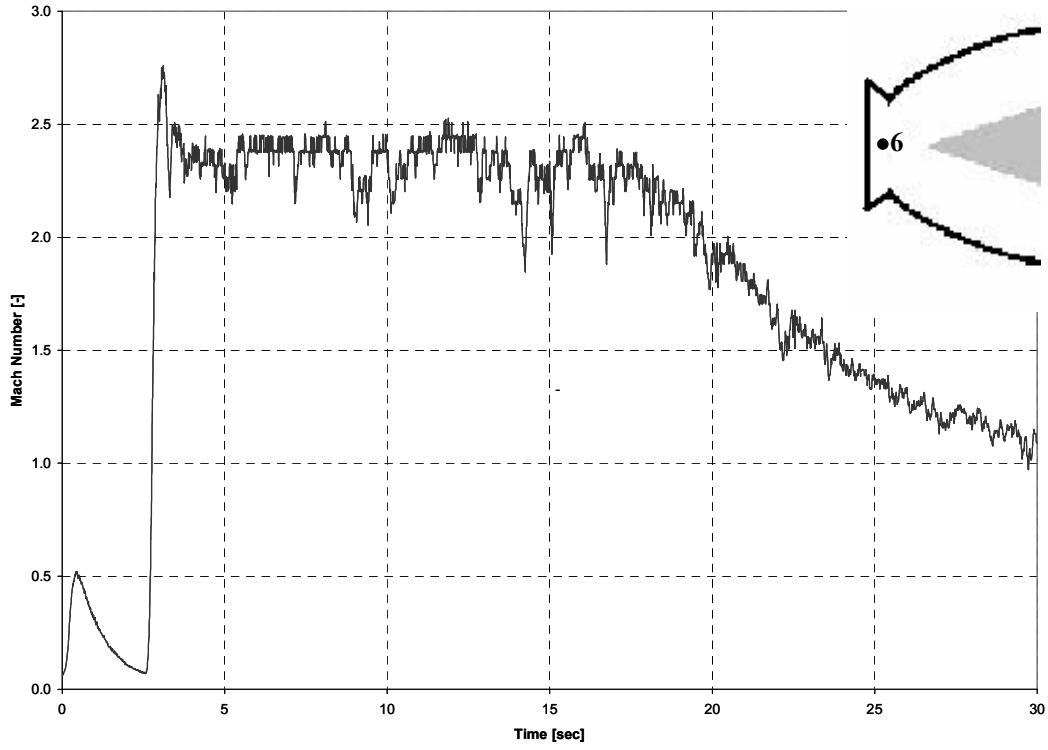

Figure 4.24 Mach Number for PT6

The Mach number at PT6 shows a steady state from approximately 3 sec to 15 sec. During this time the Mach number is approximately 2.4. Since the nozzles are designed for a Mach number of 2.2, expansion must occur immediately after the nozzle exit plane to increase the Mach number before PT6. This is confirmed by the first image in Figure 4.22.

The Mach number at PT6 was also calculated using the isentropic pressure relationship shown in Eq (3). Figure 4.25 shows a plot of Mach number calculated using Eqs. (2) and (3) at PT6 during the steady state portion of the test run.

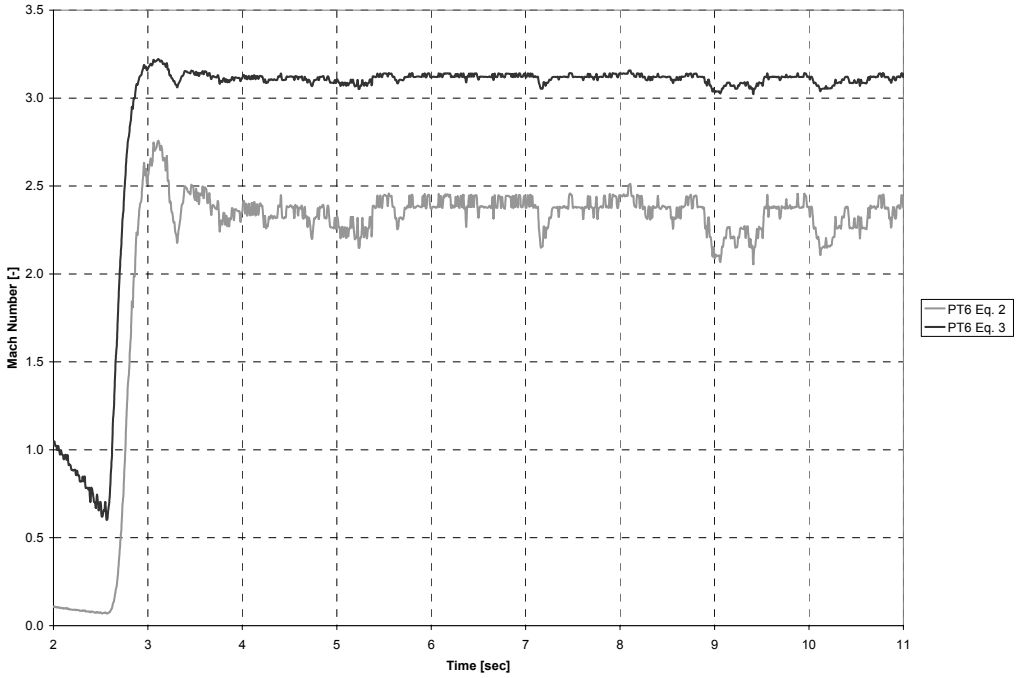

Figure 4.25 Comparison of Calculated Mach Number at PT6 Using Eqs. (2) & (3)

Without accounting for losses, the Mach number at PT6 is approximately 3.1 during its steady state time. The Mach numbers calculated using Eq. (2) are approximately 20-25% lower than the ones calculated from Eq. (3). This difference is slightly higher than the 15-20% difference found in the circular nozzle array. This is again probably due to the iteration on temperature during the steady state and the measurement of the cross-

sectional area. If losses are again assumed to be 15%, Eq. 3 shows that the nozzle exit velocity was approximately Mach 2.6. This is slightly lower than the Mach 2.7 recorded by PT1 in the circular nozzle array. However, the error in a Mach number calculation is +/- 0.1, and could be the reason for the difference.

V. Conclusions and Recommendations

First Objective-Remodel Transition Section

The first objective was to remodel the previous test facility's transition section so that it would increase run time and be capable of investigating flow conditions in a simulated laser nozzle assembly and lasing cavity using cold-flow. The facility was designed to be modular for the purposes of testing various geometries. The choke point in the previous transition structure was deemed the cause for the brevity of the transient oblique shock wave within the lasing cavity. The transition structure was not part of the SBL IFX, but was a necessary means to mate the test section to the AFIT wind tunnel. The transition structure needed to be redesigned to allow for wind tunnel startup (Bergren, 2002:5-1).

The transition section was remodeled to capture more area of the vacuum line entrance. This meant forming the transition section to mate with a rectangular diffuser exit at its entrance and a circular vacuum line entrance at its exit. This rectangle-to-circle transition section nearly captured all of the vacuum line cross-sectional area, and obtained a near 1 to 1 area ratio from its entrance to exit.

Previous results obtained with the old transition section showed an oblique shock wave attached to the leading edge of the centerbody inside the optical cavity for only 0.2 sec. For test purposes to acquire data and to simulate the conceptual design, the oblique shock wave needed to remain in the cavity for a significantly longer period of time. This is the time where the Mach number is at its highest. As stated earlier, a high Mach number is consistent with low pressure, density, and temperature. These are all desirable in the optical cavity.

After making the above changes to the transition section, this first objective was met with high success. The length of time the oblique shock wave was present in the lasing cavity increased dramatically. The transient interval time jumped from 0.2 seconds to approximately 10 sec-an increase by two orders of magnitudes.

Second Objective-Examine Flow Field

The second objective of this research was to examine the flow properties of the scaled nozzle/diffuser system. The experimental data collected from this facility could then be compared to the numerical results from TRW. This was accomplished through a combination of pressure readings and schlieren imaging at various locations throughout the diffuser.

The pressure readings were used to map Mach numbers at different locations inside the diffuser. In addition to the transducer locations recorded in the previous study, transducers were added near the nozzle exit plane and immediately downstream of the centerbody's leading edge. Near the nozzle exit, the flow traveled near Mach 2.7. However, the flow was at its highest at the leading edge of the centerbody traveling at approximately Mach 2.8. After the initial oblique shock wave, flow still remained supersonic near Mach 1.5 around the centerbody. Subsonic flow did not occur until the trailing edge of the centerbody was reached. Pressure transducers at the trailing edge and the diffuser exit plane showed subsonic flows for the entire time during all test runs. This indicated the diffuser must be working properly.

The schlieren images captured during the test runs revealed even more valuable information. As stated earlier, images of the oblique shock wave at the leading edge were captured. This allowed for the calculation of Mach number at that point. This was

then compared to the pressure analysis to confirm the readings. The Mach numbers match to within 4%. Other points of interest were the radial and horizontal expansion waves within the optical cavity (region between nozzles and centerbody leading edge). This revealed that the nozzles were underexpanded, since the flow was still expanding inside the optical cavity. After the back pressure had driven the oblique shock wave upstream near the nozzle exit, the nozzles then became overexpanded as could be seen by the dark normal shock waves at the exit.

In viewing area 2, the upper and lower half of the initial oblique shock wave was present, and a second shock wave was seen near the turning radius of the centerbody downstream of the leading edge for both the straight and circular nozzle arrays. This second shock wave revealed that the rising back pressure had a major influence on the flow characteristics upstream.

The straight nozzle array allowed visualization of the flow from a top-bottom angle 90 deg to that of the circular array. The interactions between the jets confirmed that the flow was underexpanded at the nozzle exit. Furthermore, the Mach numbers at the leading edge of the centerbody for both arrays were nearly identical during the steady state portion of each test run. Since the Mach numbers near the exit plane for both nozzle arrays were within 10% during steady state conditions, it could be concluded that the flow exiting both nozzle arrays were similar.

Similarities were also noticed between the captured schlieren images and the results from TRW's CFD analysis. First, both revealed oblique shock waves attached to the leading edge of the centerbody. Second, the streamlines interpreted in the lasing cavity from the schlieren images match closely to those in the CFD results. Finally, the

numerical results show the flow around the midsection of the airfoil to be supersonic, agreeing with the experimental results.

Although there were many similarities, there were just as many differences. The Mach number at the leading edge of the CFD results was approximately 2.3, while the test runs resulted in a Mach number of 2.8. Another difference in the shock wave was in the direction each wave bent. The numerical shock wave bent downstream as it moved closer to the outer walls, while the experimental wave bent upstream towards the nozzle array. These differences can be mostly attributed to the rising back pressure in the experimental results and discrepancies between the geometries of the subscale model and conceptual design.

Recommendations

The following is a list of prioritized improvements that can be made to the existing test facility to accomplish the original objectives to a fuller extent:

1. Perform CFD analysis simulating a rising back pressure. Also, CFD results at the exit plane of the straight nozzles should also obtained.
2. Obtain schlieren through the top and bottom of the test facility with circular nozzles.
3. Place total pressure probes at all static pressure transducer locations to obtain Mach numbers without having to iterate on temperature.
4. Replace the pressure reducer with one that can regulate the reservoir pressure at a lower range.
5. Use more pressure transducers in the optical cavity to accurately map the flow velocities in the entire area.

Appendix A: Calculation of Losses Through Non-Isentropic Nozzle (Bergren, 2002)

To gain knowledge of what types of losses will occur with a non-contoured nozzle wall, a single nozzle was manufactured. The nozzle built was simply a linear nozzle and unlike the nozzles created for the model. It was created with no contour in the nozzle wall. The expansion ratio was 1.44 and would have yielded a Mach number of 1.8.

The nozzle was bolted to the wind tunnel stilling chamber with the exit open to the atmosphere. A stagnation pressure of 35 psi in the stilling chamber resulted in a pressure ratio across the nozzle of approximately 2.5 when venting to atmosphere.

A schlieren picture was projected onto a white piece of cardboard. A small metal wedge was placed in the flow (1 mm away from the nozzle exit plane) with a half angle of 7.5 degrees. Once the flow started, an oblique shock wave was created off the leading edge of the wedge at an unknown angle. The picture was sketched onto the cardboard while the wind tunnel was running. The shock wave angle was measured with a protractor to be 53-degrees. Knowing the relationship between the wedge half angle and the angle of the shock wave, the Mach number at the wedge was estimated to be Mach 1.5. Due to losses inside the sample nozzle, a 15% deviation from the isentropic expansion Mach number can be deduced.

Appendix B: Uncertainty Analysis (Bergren, 2002)

An uncertainty analysis was performed for the instrumentation used to determine the accuracy for a single pressure reading. This analysis was provided by Wheeler and Ganji (178-182). The following is a list of calibration errors broken down by instrumentation component. The Full Scale (FS) of the transducers was 50 psia.

Pressure Transducer:

Nonlinearity and hysteresis = +/- 0.1% FS

Repeatability = +/- 0.1% FS

Thermal sensitivity shift = +/- 0.015%/^{0}F

Pressure Signal Conditioner:

Gain error = +/-0.5% FS

The calibration errors were categorized into bias and precision uncertainties. The only bias error in the system due to the pressure transducer was the nonlinearity and hysteresis uncertainties and found to be:

$$B_1 = \frac{0.1}{100}(50\,psia) = \pm 0.05\,psia$$

The precision error due to the pressure transducer was from the repeatability and thermal sensitivity shift. To ensure the uncertainty was with a 95% confidence level, the degrees of freedom were assumed to be 30. When referencing a tabulated form of the Student's t-distribution, t = 2. The precision indices could be estimated:

$$S_{repeatibility} = S_1 = \frac{(0.1\%)(FS)}{(100)t} = 0.025\,psia$$

$$S_{thermal} = S_2 = \frac{(0.015)(T_{shift})(FS)}{(100)t} = 0.0075\,psia \text{ where } T_{shift} = \pm 2^0 F\,.$$

The single uncertainty of the signal conditioner was a bias uncertainty. The error was calculated:

$$B_{gain} = B_2 = \frac{(\pm 0.5\%)(FS)}{100} = 0.25\,psia$$

By combining all the bias and precision errors of the system, a total bias and precision error was calculated:

$$B_T = \left(B_1^{\,2} + B_2^{\,2}\right)^{\frac{1}{2}} = 0.255\,psia$$

$$S_T = \left(S_1^{\,2} + S_2^{\,2}\right)^{\frac{1}{2}} = 0.0261\,psia$$

Finally, the estimated uncertainty for a single pressure reading could be found:

$$\boxed{w_T = \left(B_T^{\,2} + tS_T^{\,2}\right)^{\frac{1}{2}} = 0.261\,psia = 1793\,Pa}$$

Therefore, the uncertainty in a pressure reading was $\pm 0.3\,psia$ (2000 Pa) with 95% confidence level considering significant figures.

Calculated Results:

The maximum error in the calculations performed for mass flow and Mach number was investigated considering the uncertainty in pressure. Recall the mass flow equation:

$$\dot{m} = \frac{p_t}{\sqrt{RT_t}} A\sqrt{\gamma}\left(1 + \frac{\gamma - 1}{2} M^2\right)^{\frac{\gamma+1}{2-2\gamma}}$$

Taking the partial derivative with respect to the total pressure, and applying the equation to the nozzle throat:

$$\frac{\partial \dot{m}}{\partial p_t} = \frac{A\sqrt{\gamma}\left(1+\frac{\gamma-1}{2}M^2\right)^{\frac{\gamma+1}{2-2\gamma}}}{\sqrt{RT}} = 2.61E-6$$

$$w_{p_t} = 1793Pa$$

Therefore, the max error in the mass flow calculations was determined to be:

$$w_{\dot{m}} = \frac{\partial \dot{m}}{\partial p_t} w_{p_t} = (2.61E-6)(1793)$$
$$w_{\dot{m}} = 4.7E-3kg/s$$

The Mach number equation is:

$$M = \frac{\dot{m}RT}{pA\sqrt{\gamma RT}}$$

The sources of error in this equation are due to the mass flow calculation, uncertainty in pressure reading, and temperature fluctuations. The temperature within the test section was assumed to range +/- 10 K during the run.

$$w_T = 10K$$
$$w_p = 1763Pa$$
$$w_{\dot{m}} = 4.68E-3kg/\sec$$
$$\frac{\partial M}{\partial \dot{m}} = 2.97$$
$$\frac{\partial M}{\partial p} = -3.33E-5$$
$$\frac{\partial M}{\partial T} = 0.0015$$

To find the maximum error in Mach number:

$$w_M = \frac{\partial M}{\partial \dot{m}} w_{\dot{m}} + \frac{\partial M}{\partial p} w_p + \frac{\partial M}{\partial T} w_T$$
$$w_M = 0.1$$

Appendix C: Calculation of Vacuum Supply Line Head Loss

These calculations determined the initial pressure rise in the 73-foot long vacuum line when the compressed air was released through the test section. The pressure in the vacuum supply line was used to determine velocity and density. The cross-sectional area at this location was 0.174 m^2 (270 in^2).

Calculate mass flow at the nozzle throat:

$$\dot{m} = \frac{p_0 A^*}{\sqrt{T_0}} \sqrt{\frac{\gamma}{R}\left(\frac{2}{\gamma+1}\right)^{(\gamma+1)/(\gamma-1)}}$$

where,

γ=1.4

A^* = 0.0011 m^2

p_o = 26.5 psia = 182.71 kPa

T_o = 290 K

R = 287 KJ/kgK

M = 1

Therefore, $\dot{m}$ = 0.48 *kg/s*

By using the back pressure immediately after the initial rise in pressure as is seen in Figure 4.2:

p = 2.0 psia = 13.8 kPa

Calculate average velocity in vacuum line:

$$V = \frac{\dot{m} R T}{p\ A}$$

$$V = \frac{(0.48kg/s)(287KJ/kgK)(290K)}{(13800Pa)(0.174m^2)}$$

$$V = 16.64m/s$$

Assuming the flow was incompressible, determine the velocity in the vacuum line at the location immediately downstream of where the transducer was located.

$$V_{line} = \frac{V\ A}{A_{line}}$$

where $A_{line} = 44.2in^2 = 0.028m^2$

$$V_{line} = \frac{(16.64m/s)(0.174m^2)}{(0.028m^2)}$$

$$V_{line} = 103.41m/s$$

Determine Reynolds number to classify flow as turbulent or laminar.

$$\mathrm{Re}_D = \frac{\rho VD}{\mu}$$

Using Sutherland's Law, find μ.

$$\mu = \frac{bT^{\frac{3}{2}}}{S+T}$$

where,

b=1.458E-6 and

S=110.4 K

μ = 1.82E-5 Ns/m^2

Calculate the density using the ideal gas law.

$$\rho = \frac{p}{RT} = \frac{13800Pa}{(287kJ/kgK)(290K)} = 0.166kg/m^3$$

Therefore,

$$\mathrm{Re}_D = \frac{(0.166 kg/m^3)(103.41 m/s)(0.1905 m)}{1.82E-5 Ns/m^2}$$

$$\mathrm{Re}_D = 179{,}678$$

The transition Reynolds number for pipe flow is roughly 2,000. Therefore, the flow was turbulent inside the vacuum line. Calculate the losses caused by friction:

$$h_l = f\frac{L}{D}\frac{\overline{V^2}}{2}$$

A friction factor of 0.03 was used. Therefore,

$$h_l = (0.03)\frac{(22.25 m)}{(0.1905 m)}\frac{(103.41 m/s)^2}{2}$$

$$h_l = 18{,}735 m^2/s^2$$

The minor losses associated with pipe bends were determined:

$$h_{lm} = f\frac{L_e}{D}\frac{\overline{V}^2}{2}$$

where the L_e/D is the equivalent length. For the six 90 deg elbows with a radius of 1 foot, the equivalent length used equals 25. The two 45 deg elbows, the equivalent length of 12 was used (Fox, 1992).

$$h_{lm} = (0.02)\frac{(103.41)^2}{2}[6(25)+2(12)]]$$

$$h_{lm} = 18{,}607 m^2/s^2$$

Furthermore, sudden contractions and expansions were factored into the overall losses.

A sudden contraction occurs from the void where the transducer was located to the vacuum line. The contraction ratio $\frac{A_{line}}{A} = 0.164$. An expansion exists at the end of the vacuum line when the fluid was dumped into the 6000-gallon cylindrical vacuum tank. The expansion ratio was $\frac{A_{line}}{A_{\tan k}} = 0.016$. Using Equation (14) and looking up the loss coefficients based on the contraction/expansion ratios (Bergren, 2002):

$$h_{l,e/c} = \frac{\overline{V}^2}{2}(K_e + K_c)$$

$$h_{l,e/c} = \frac{(103.41)^2}{2}(0.9 + 0.45)$$

$$h_{l,e/c} = 7{,}218 m^2/s^2$$

Add all three types of losses together,

$$h_{l,T} = 44560 m^2/s^2$$

Transform head loss into a change in pressure:

$$\Delta p = h_{l,T}\rho = (44560 m^2/s^2)(0.166 kg/m^3)$$

$$\Delta p = 7{,}397 Pa = 1.1 psi$$

Appendix D: Back Pressure Analysis

Using conservation of mass and the ideal gas law, the following equation relating rate of change in pressure to mass flow can be derived.

$$\frac{dp}{dt} = \frac{RT\dot{m}}{\Lambda}$$

where the vacuum tank had a volume of 6000 gallons.

$\Lambda = 6000$ gallons = $22.71 m^3$

Therefore, using the mass flow found in Appendix D and assuming temperature was constant at room temperature,

$$\frac{dp}{dt} = \frac{(287 KJ/kgK)(290 K)(0.48 kg/s)}{22.71 m^3}$$

$$\frac{dp}{dt} = 1759.15 Pa/s$$

$$\frac{dp}{dt} = 0.26 psi/s$$

Appendix E: Englarged Images of Oblique Shock Wave Motion in Area 1

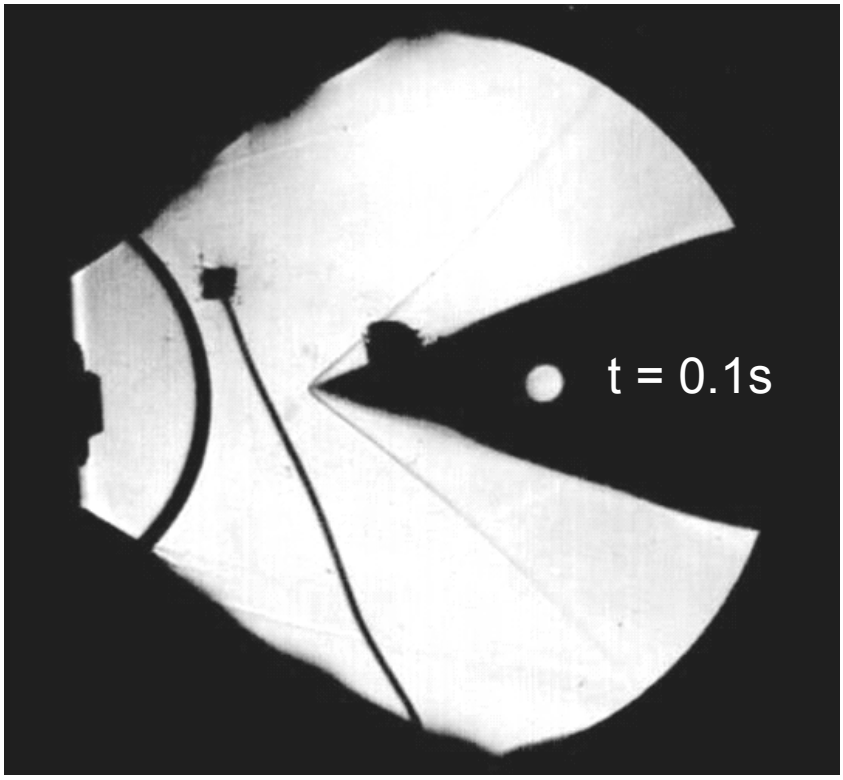

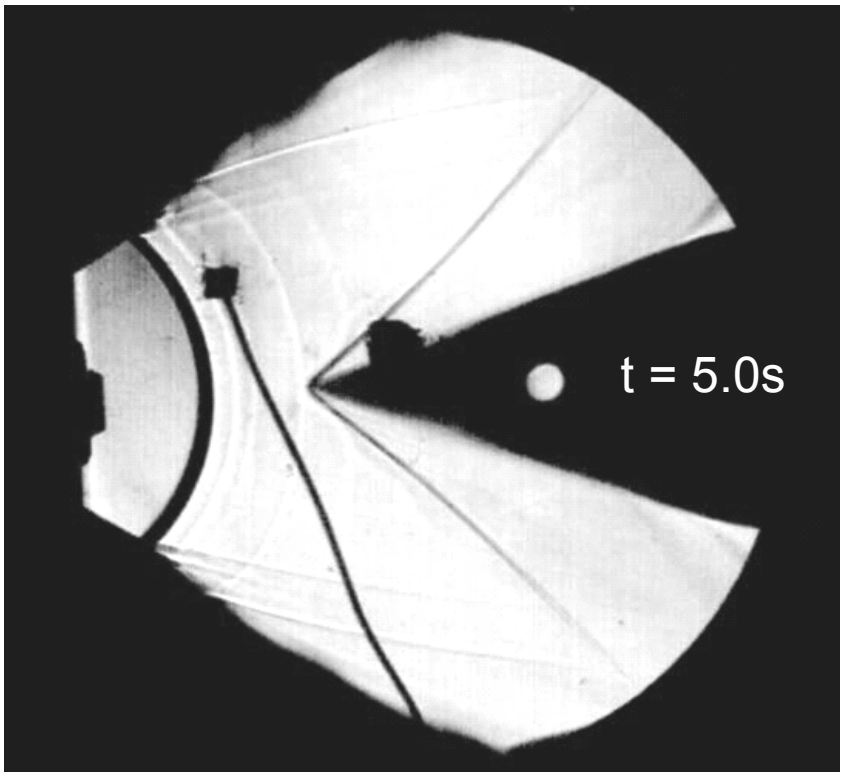

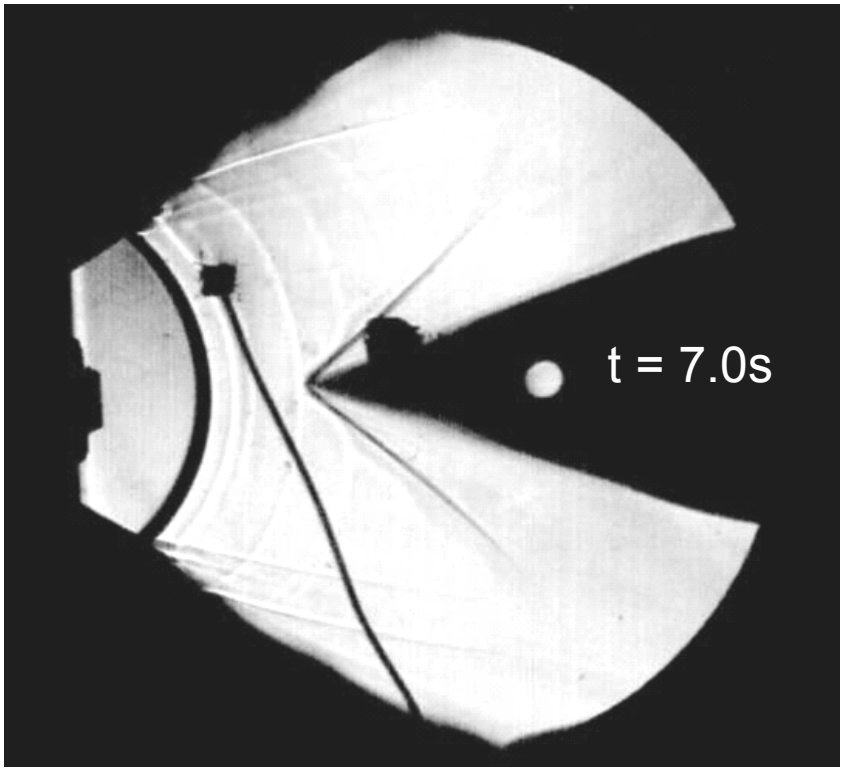
t = 7.0s

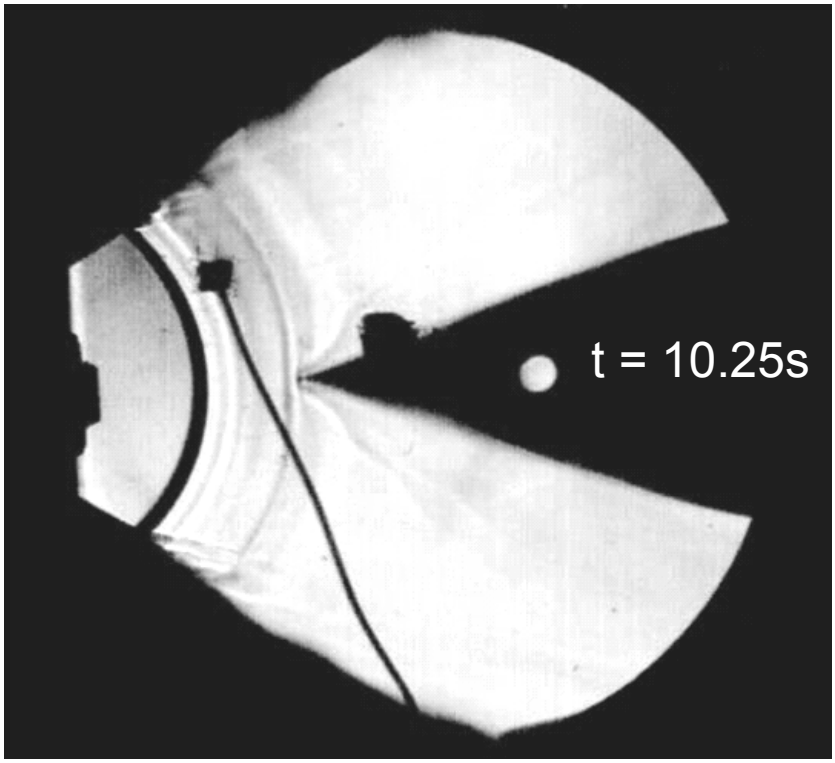
t = 10.25s

Appendix F: Pressure and Mach Number Calculations at PT2

The pressure and Mach number behind an oblique shock wave can be found using the θ–β-*M* relation described in Chapter 3. Below is a drawing of the radial flow exiting the nozzle array.

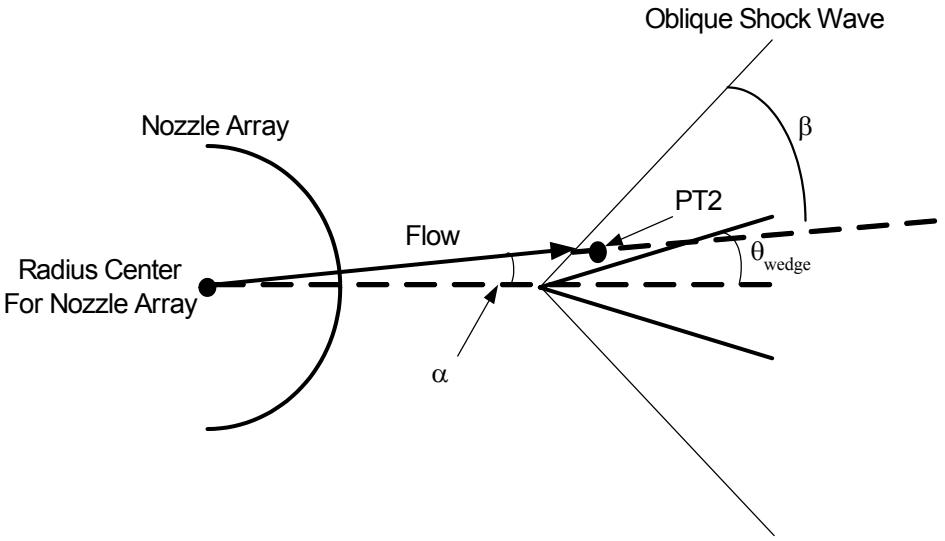

For the flow approaching PT2 during the steady state period,

$\alpha = 5$ deg

$\theta_{wedge} = 21$ deg

$\beta = 40$ deg

Since the flow is at a 5 degree angle relative to the centerline, the turning angle becomes

$\theta = \theta_{wedge} - \alpha = 16\,\text{deg}$

Using plots derived from the θ–β-*M* relation, M = 2.35

The next step is to determine the velocity component normal to the oblique shock wave.

$M_{n_1} = M_1 \sin\beta$ Therefore,

$M_{n_1} = 2.35 * \sin 40 = 1.51$

Then, normal shock properties can be used to find both the pressure and the normal component of the velocity behind the shock wave.

Calculate pressure behind the shock

$$p_2 = 1 + \frac{2\gamma}{\gamma + 1}\left(M_{n_1}^2 - 1\right)p_1$$

where p_1 = 2.6 kPa during the steady state period (measured from PT1).

$$p_2 = 1 + \frac{2\gamma}{\gamma + 1}\left(1.51^2 - 1\right)\cdot 2.6 = 6.5kPa$$

To find the normal component of the velocity behind the shock, use ref (Kuethe, Chow, 1998)

$$M_{n_2} = 0.7$$

Calculate the total velocity behind the shock wave

$$M_2 = \frac{M_{n_2}}{\sin(\beta - \theta)} = \frac{0.7}{\sin(40 - 15)} = 1.65$$

These calculations can be used at any location along the oblique shock wave shown in Figure 4.19. As the location moves up along the shock wave, α increases, which causes the turning angle, θ, to decrease. Once the shock wave angle, β, is measured, the upstream Mach number can be found in tabulated tables.

Appendix G: Enlarged Images of Oblique Shock Wave Motion in Area 2

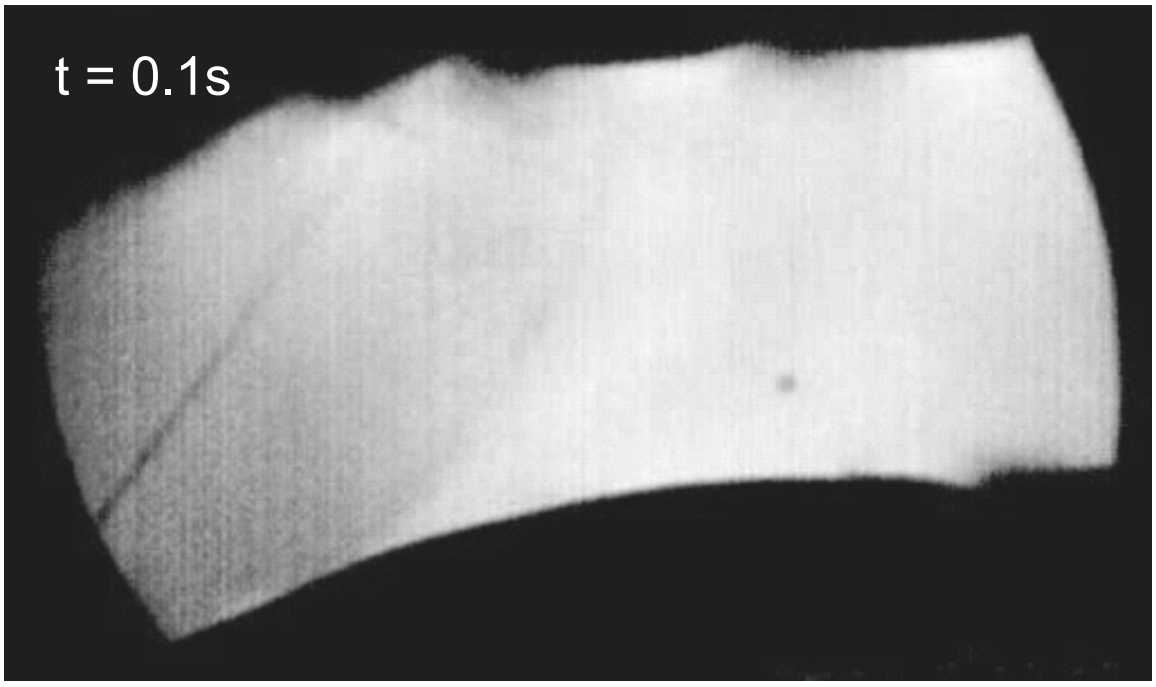

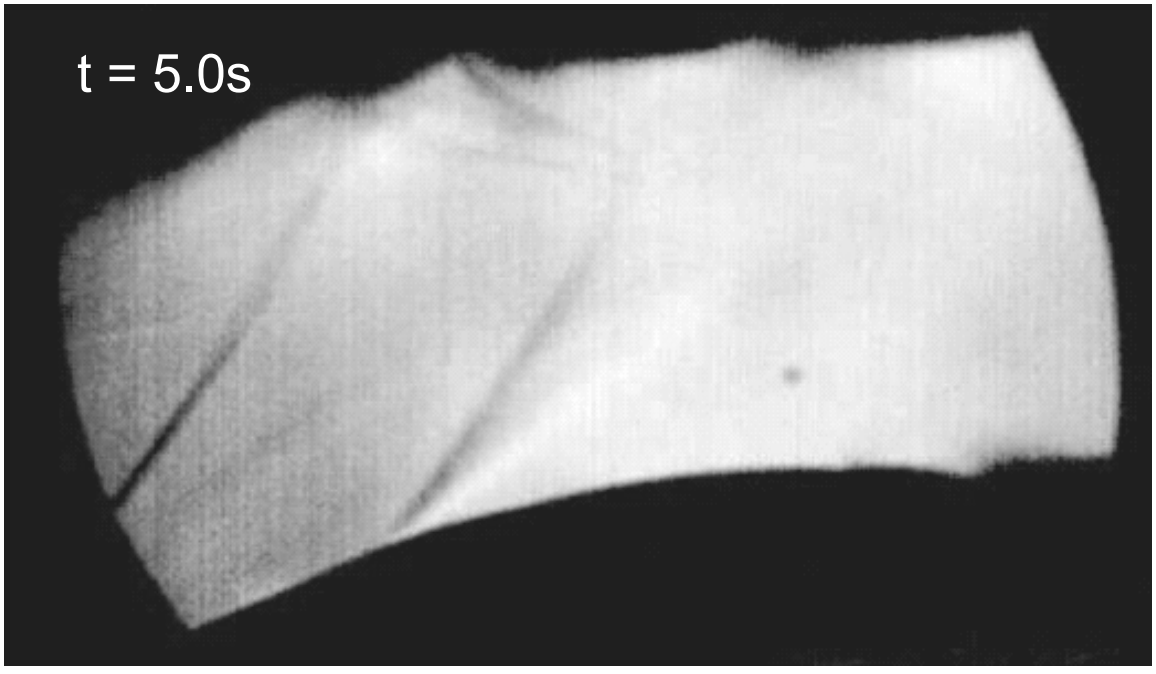

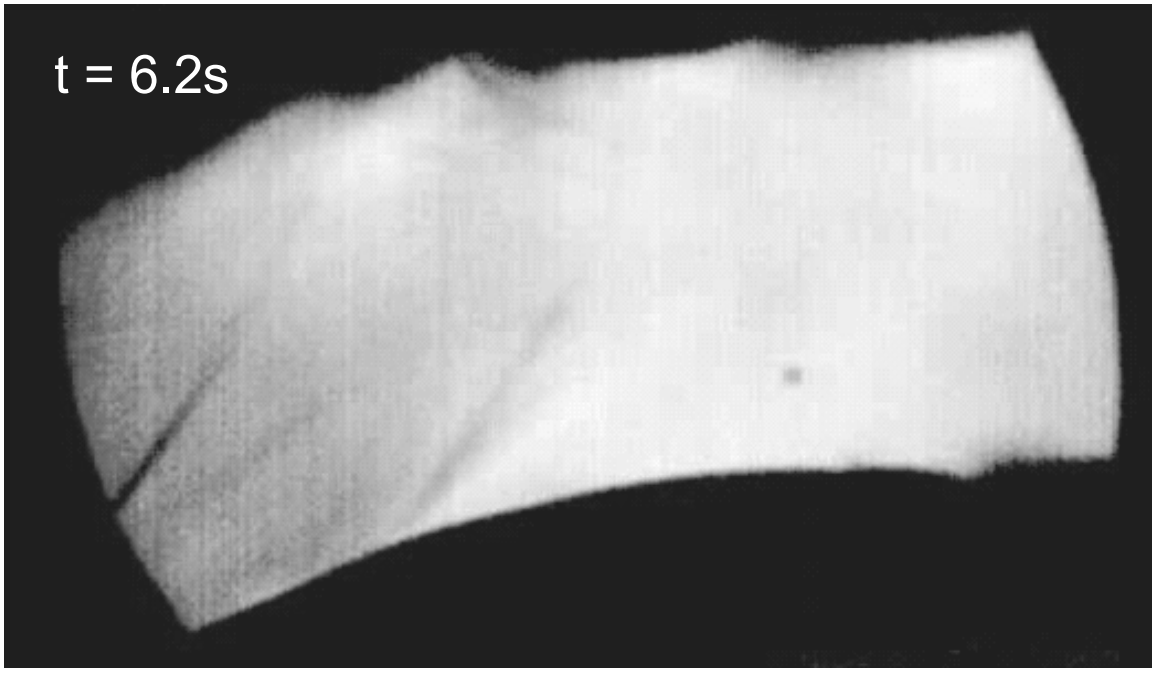
t = 6.2s

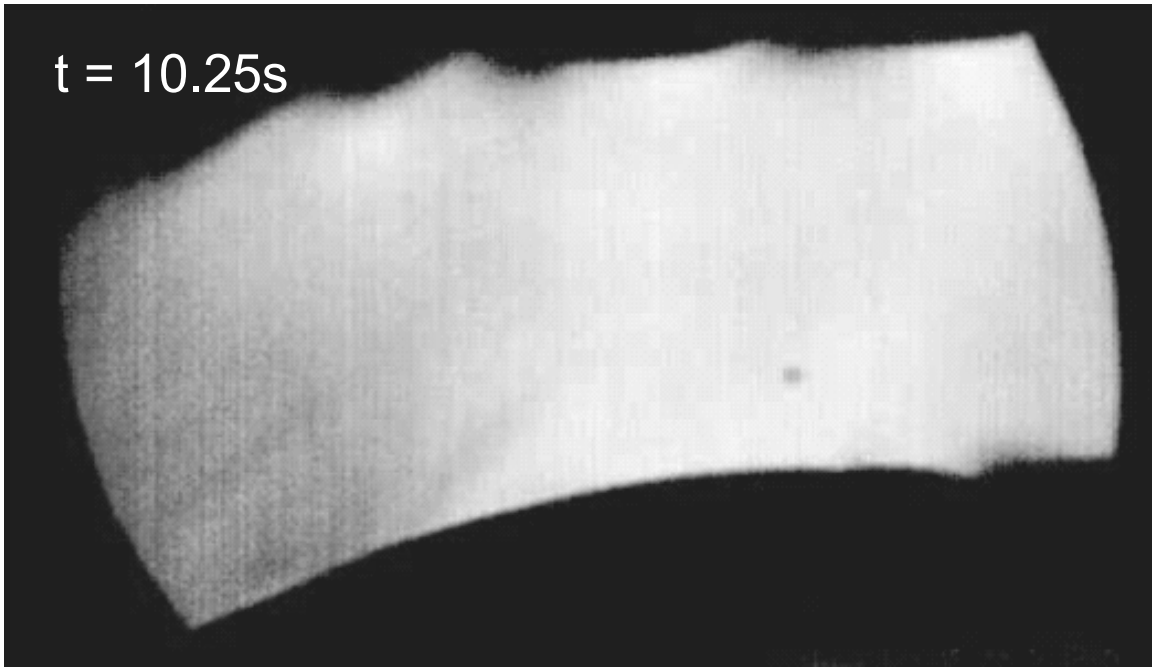
t = 10.25s

Appendix H: Enlarged Images Straight Nozzle Flow in Area 1

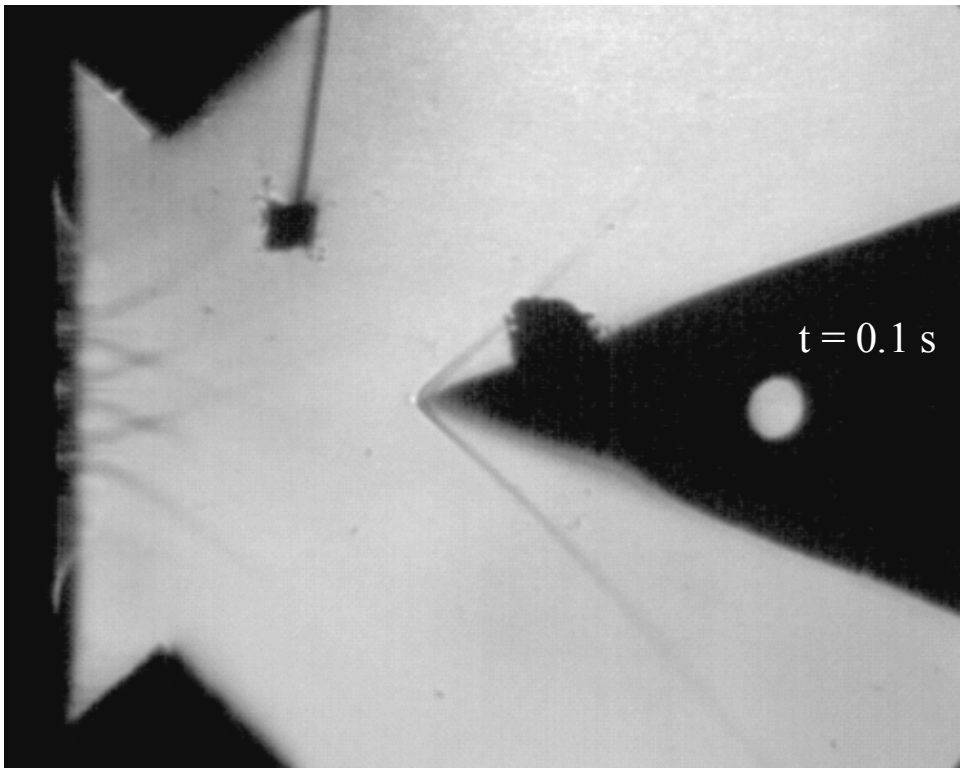

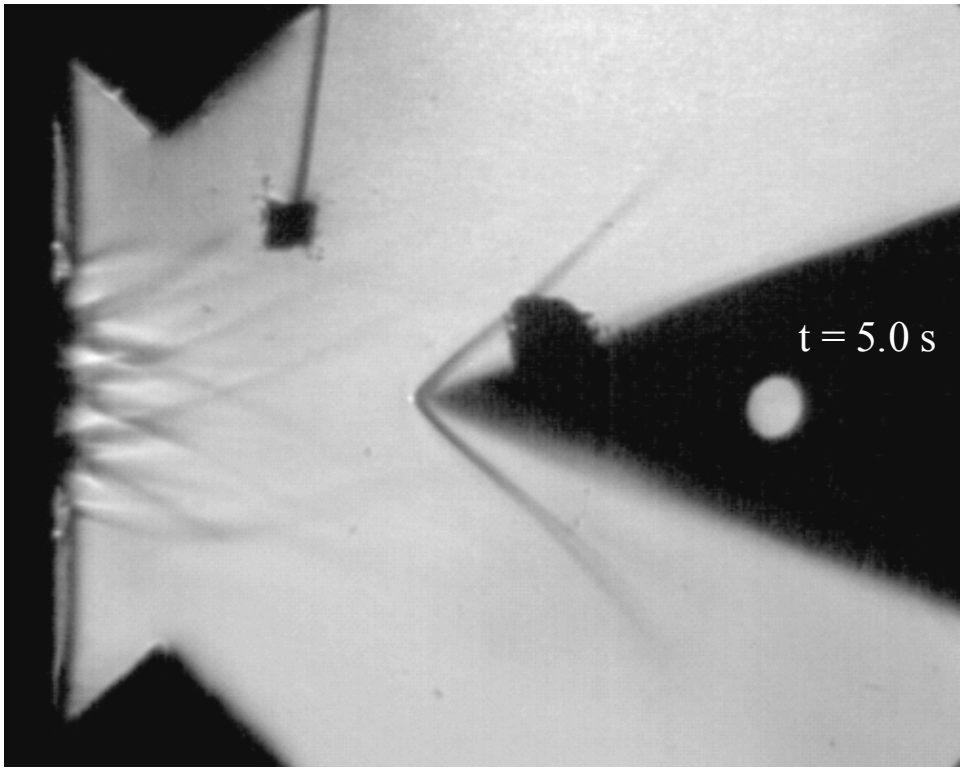

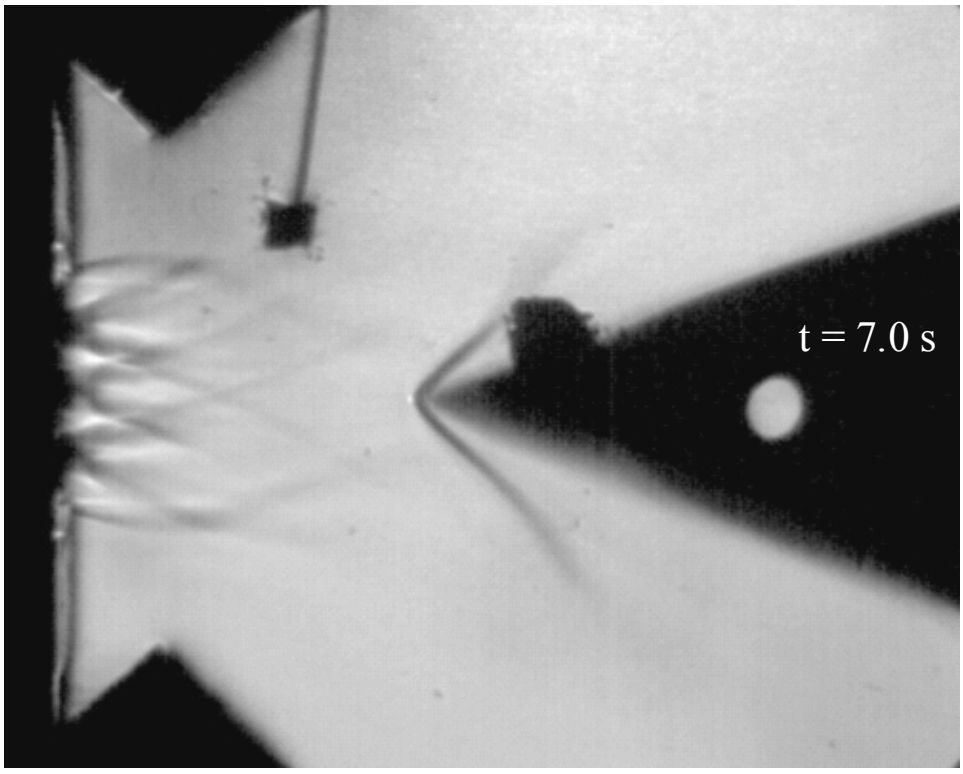
t = 7.0 s

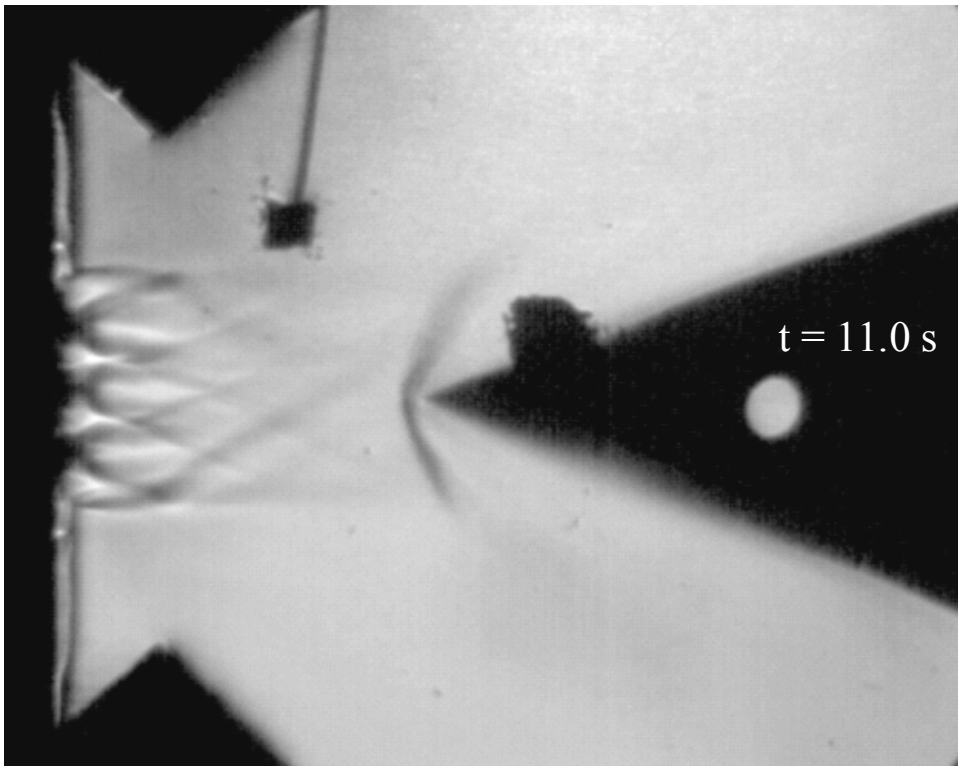
t = 11.0 s

Appendix I: Enlarged Images Straight Nozzle Flow in Area 2

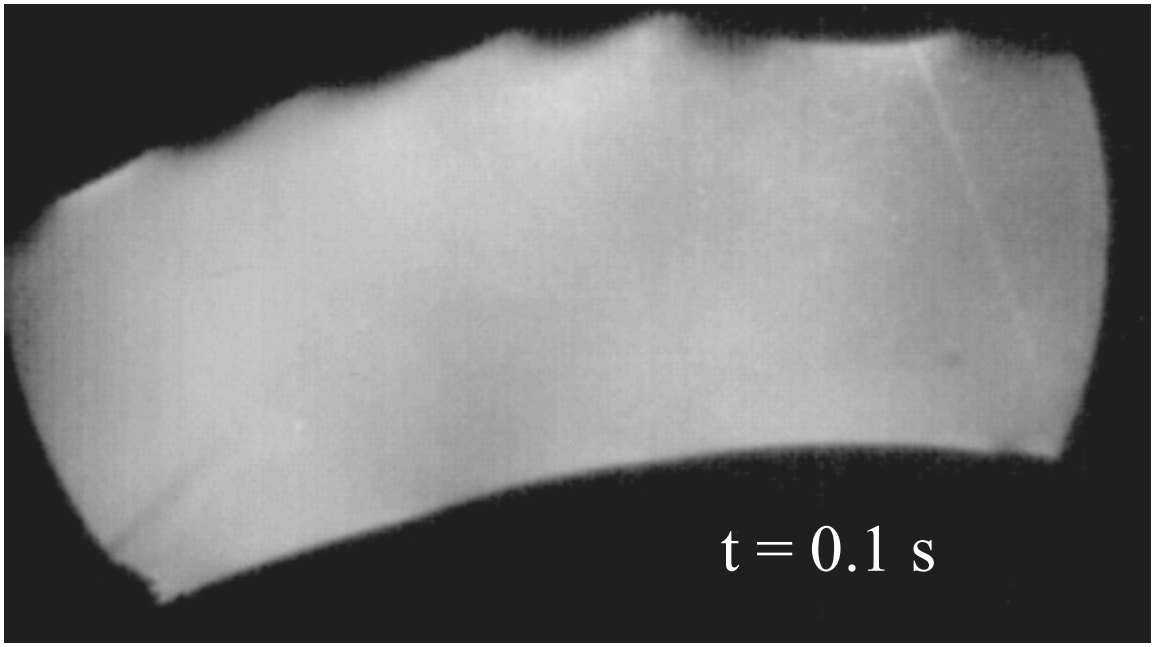

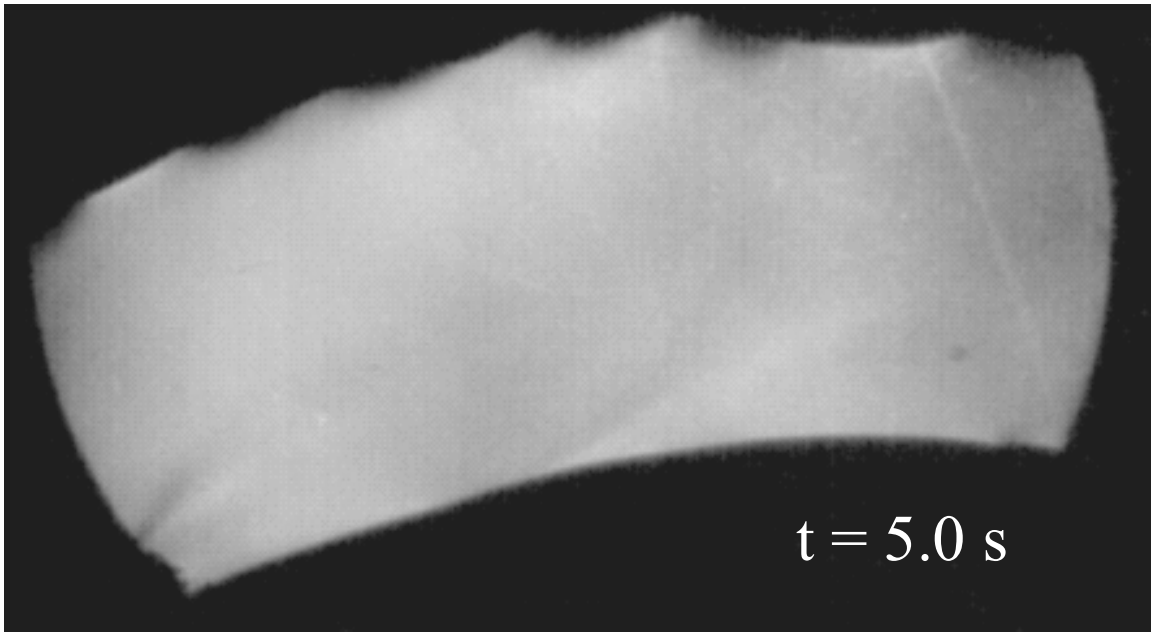

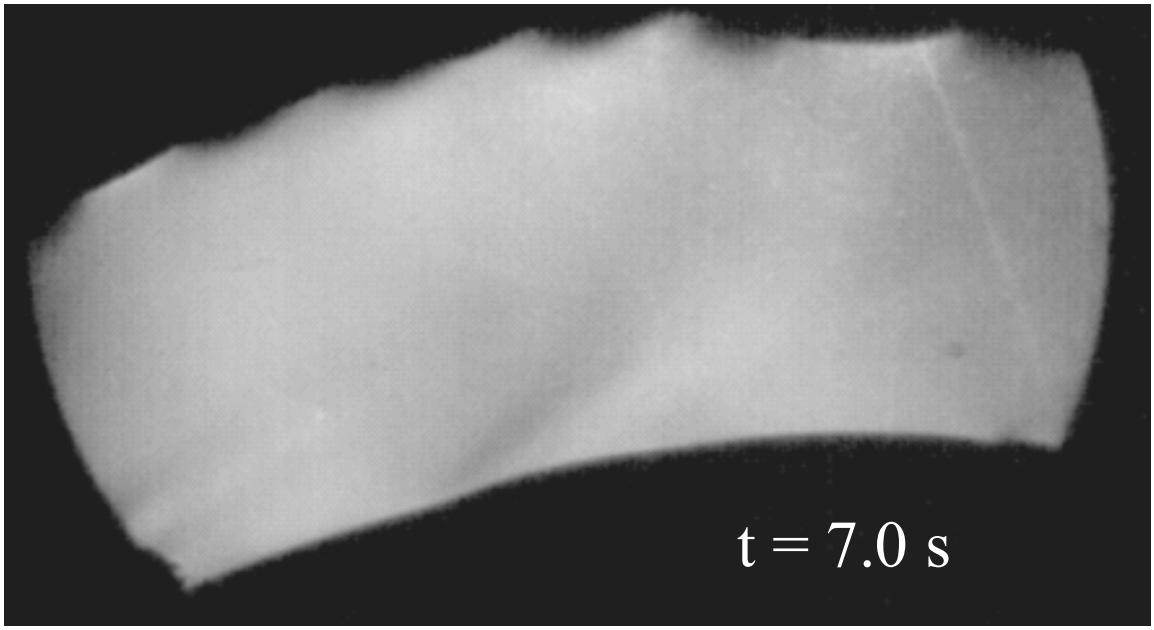
t = 7.0 s

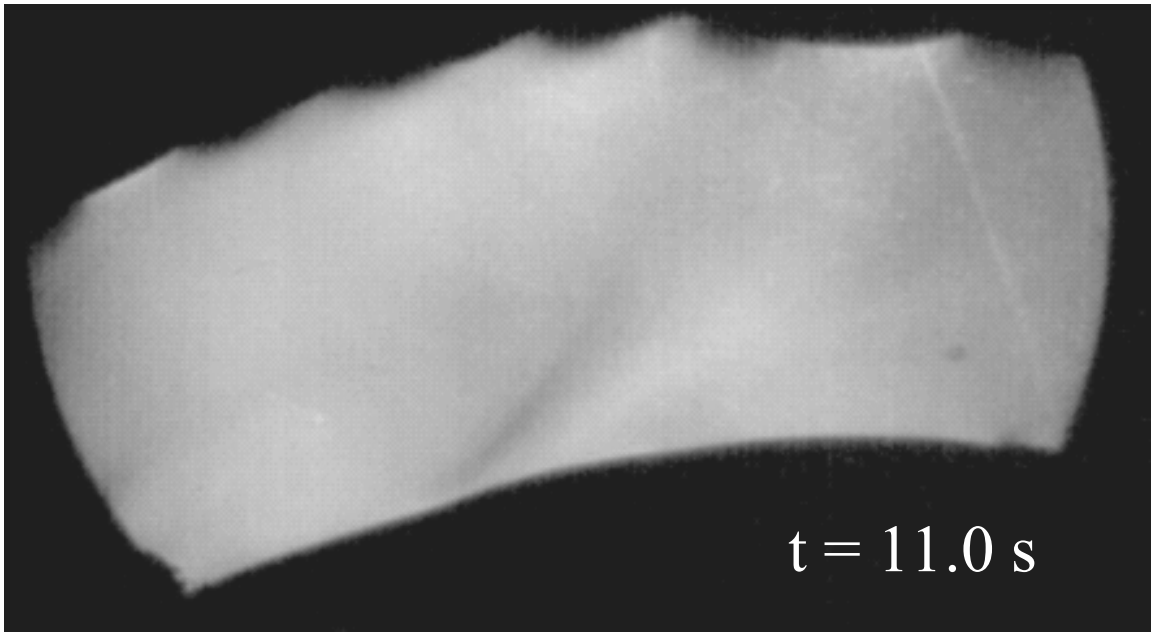
t = 11.0 s

Bibliography

Anderson, John D. Gasdynamic Lasers: An Introduction. New York: Academic Press, 1976.

Anderson, John D. Modern Compressible Flow. New York: McGraw-Hill, 1990.

Bergren, Scott. Fabrication and Cold-Flow Testing of Subscale Space-Based Laser Geometry. Unpublished Thesis. Wright-Patterson Air Force Base, OH: Air Force Institute of Technology, 2002.

Bjurstrom, David R. An Experimental Study of Clustered, Two-Dimensional Rocket Nozzles. Unpublished Thesis. Wright-Patterson Air Force Base, OH: Air Force Institute of Technology, 1984.

Federation of American Scientists. "Space Based Laser (SBL)", 2002. http://www.fas.org/spp/starwars/program/sbl.htm

Fox, Robert W. and McDonald, Alan T. Introduction to Fluid Mechanics, 4th ed. New York: John Wiley and Sons, Inc., 1992.

Goethert, Bernard H. Studies of the Flow Characteristics and Performance of Multi-Nozzle Rocket Exhausts. AEDC-TR-59-16. Arnold AFS, TN: ARO, Inc., October 1959.

Greenwald, John. "Megawatt Laser Test Brings Space Based Lasers One Step Closer", 2000. http://www.blackvault.com/space_laser.html

Kuethe, Arnold and Chow, Chuen-Yen. Foundations of Aerodynamics. New York: John Wiley and Sons Inc, 1998.

Lohn, Peter of TRW, Inc, Fluid and Thermophysics Department, Redondo Beach, CA. "Personal interviews," 2001.

Pai, Shih-I. Fluid Dynamics of Jets. Toronto: D. Van Nostrand Company, Inc, 1954.

Perram, Glen P. "Chemical Lasers," Web Page Tutorial, 1999. http://en.afit.edu/enp/Faculty/perram.html

Sleigh, Andrew. "Similarity and Modeling," 2001. http://www.efm.leeds.ac.uk/CIVE/CIVE1400/Section5/similarity.htm

White, Frank M. Viscous Fluid Flow. Boston: McGraw-Hill, 1991.

Wheeler, Anthony J., Ganji, Ahmad R. Introduction to Engineering Experimentation. New Jersey: Prentice Hall, 1976.

Vita

Captain Ian Bautista graduated from Yokota High School in Yokota Air Base, Japan. He entered undergraduate studies at the United States Air Force Academy, Colorado Springs, Colorado where he graduated with a Bachelor of Science degree in Aeronautical Engineering in May 1998.

His first assignment was at the U.S. Air Force Academy 10th Communications Squadron as a Network Engineer in August 1998. In May 1999, he was assigned to the Warner Robins Air Logistics Center, C-130 SPO, Robins AFB, Georgia where he served as an Aerospace Structural Engineer. In August 2001, he entered the Graduate School of Engineering and Management, Air Force Institute of Technology. Upon graduation, he will be assigned to the Munitions Directorate at Eglin AFB, Florida.

REPORT DOCUMENTATION PAGE

Form Approved
OMB No. 074-0188

1. REPORT DATE *(DD-MM-YYYY)*	2. REPORT TYPE	3. DATES COVERED *(From – To)*
25-03-2003	**Master's Thesis**	Jul 2002 – Mar 2003

4. TITLE AND SUBTITLE
COLD-FLOW TESTING OF A SUBSCALE MODEL EXHAUST SYSTEM FOR A SPACE-BASED LASER

5a. CONTRACT NUMBER
5b. GRANT NUMBER
5c. PROGRAM ELEMENT NUMBER

6. AUTHOR
Bautista, Ian S., Capt, USAF

5d. PROJECT NUMBER
5e. TASK NUMBER
5f. WORK UNIT NUMBER

7. PERFORMING ORGANIZATION NAMES(S) AND ADDRESS(S)
Air Force Institute of Technology
Graduate School of Engineering and Management (AFIT/ENY)
2950 Hobson Way, Building 642
WPAFB OH 45433-7765

8. PERFORMING ORGANIZATION REPORT NUMBER
AFIT/GAE/ENY/03-1

9. SPONSORING/MONITORING AGENCY NAME(S) AND ADDRESS(ES)
SMC/TL
Attn: 1st Lt William Welser
14800 Aviation Blvd. DSN: 833-2524
Lawndale, CA 92960 email: William.Welser@losangeles.af.mil

10. SPONSOR/MONITOR'S ACRONYM(S)
11. SPONSOR/MONITOR'S REPORT NUMBER(S)

12. DISTRIBUTION/AVAILABILITY STATEMENT
APPROVED FOR PUBLIC RELEASE; DISTRIBUTION UNLIMITED.

13. SUPPLEMENTARY NOTES

14. ABSTRACT
The purpose of this research was to continue a study of gas-dynamic phenomena that occurred in stacked cylindrical rings of nozzles and an exhaust manifold as reported by Captain Scott Bergren in 2002. The rings and exhaust manifold were part of a 1/5-scale model of one quadrant of the conceptual Space Based Laser Integrated Flight Experiment (SBL IFX) gas dynamic laser. This model was mated to a blow-down/vacuum wind tunnel and consisted of a nozzle array, centerbody, supersonic diffuser, and a transition structure to mate the vacuum and test section. The objectives of this research were to remodel the transition structure of the test section in order for the facility to simulate the expected fluid flow properties in the conceptual SBL IFX design using cold-flow, and to evaluate its performance. The transition structure was remodeled to capture the entire vacuum line entrance area while still mating to the diffuser exit. Using rapid data acquisition and schlieren photography, results indicated that supersonic flow lasted for 10.25 seconds from startup. During this time, a well-defined oblique shock wave inside the lasing cavity attached to the leading edge of the centerbody, and the flow reached a velocity of Mach 2.7.

15. SUBJECT TERMS
Laser Applications, Space Defense, Space Technology, Fluid Flow

16. SECURITY CLASSIFICATION OF:			17. LIMITATION OF ABSTRACT	18. NUMBER OF PAGES	19a. NAME OF RESPONSIBLE PERSON
a. REPORT	b. ABSTRACT	c. THIS PAGE			Dr. Milton E. Franke (ENY)
U	**U**	**U**	**UU**	108	**19b. TELEPHONE NUMBER** *(Include area code)* (937) 255-3636 ext 4720; email: milton.franke@afit.edu

Standard Form 298 (Rev. 8-98)
Prescribed by ANSI Std. Z39-18
Form Approved
OMB No. 074-0188